Article

Selective presynaptic inhibition of leg proprioception in behaving *Drosophila*

https://doi.org/10.1038/s41586-025-09554-2

Received: 21 June 2024

Accepted: 19 August 2025

Published online: 17 September 2025

Check for updates

Chris J. Dallmann[1,3], Yichen Luo[1], Sweta Agrawal[1,4], Akira Mamiya[1], Grant M. Chou[1], Andrew Cook[1], Anne Sustar[1], Bingni W. Brunton[2] & John C. Tuthill[1]✉

Controlling arms and legs requires feedback from the proprioceptive sensory neurons that detect joint position and movement[1,2]. Proprioceptive feedback must be tuned for different behavioural contexts[3–6], but the underlying circuit mechanisms remain poorly understood. Here, using calcium imaging in behaving *Drosophila*, we find that the axons of position-encoding leg proprioceptors are active across a range of behaviours, whereas the axons of movement-encoding leg proprioceptors are suppressed during walking and grooming. Using connectomics[7–9], we identify a specific class of interneurons that provide GABAergic presynaptic inhibition to the axons of movement-encoding proprioceptors. These interneurons receive input from parallel excitatory and inhibitory descending pathways that are positioned to drive the interneurons in a context-specific and leg-specific manner. Calcium imaging from both the interneurons and their descending inputs confirms that their activity is correlated with self-generated but not passive leg movements. Taken together, our findings reveal a neural circuit that suppresses specific proprioceptive feedback signals during self-generated movements.

Effective motor control of arms and legs requires sensory feedback from proprioceptive sensory neurons (proprioceptors) that detect the position and movement of the body[1,2]. Motor circuits in the central nervous system integrate proprioceptive information at multiple levels to support a range of motor functions, from postural stabilization to adaptive locomotion[10–12].

Because the same proprioceptors are used for many different motor-control tasks, proprioceptive feedback must be flexibly tuned to the behavioural context[3]. For example, proprioceptive feedback pathways can be inhibited during voluntary movement to prevent disruption by reflexes[6,13] or by the inherent time delays in sensory pathways[5]. An efficient means of flexibly tuning sensory feedback pathways is predictive inhibition. In theoretical frameworks of predictive inhibition[14,15], the motor circuits send an inhibitory signal to the sensory circuits that is based on the motor commands (Fig. 1a, left). This mechanism, called efference copy or corollary discharge, allows self-generated sensory signals to be attenuated or eliminated (Fig. 1a, right).

Predictive inhibition of sensory feedback has been described for many sensory modalities and species[3,14–17]. Inhibition can occur at multiple levels of the nervous system, but a common mechanism is presynaptic inhibition, in which inhibitory neurons directly target the sensory axon terminals in the spinal cord or invertebrate ventral nerve cord (VNC) to reduce neurotransmitter release[18,19]. Previous studies have shown that presynaptic inhibition can dynamically suppress sensory transmission in proprioceptive axons. For example, the axons of leg proprioceptors in mice[5,6] and locusts[4] receive GABAergic inhibition during walking and reaching, presumably driven by motor circuits. However, the extent to which specific proprioceptive feedback pathways are inhibited during behaviour, and the organization and recruitment of the underlying neural circuits, remain unknown. This is due in part to a lack of comprehensive connectivity analyses of proprioceptive circuits in the spinal cord and VNC, and the technical difficulty of recording from identified neurons in these circuits in behaving animals.

Here, we address these challenges in the fruit fly, *Drosophila melanogaster*. We focus on the femoral chordotonal organ (FeCO), which is the largest proprioceptive organ in the fly leg[20] (Fig. 1b, left). Proprioceptors in the FeCO are functionally analogous to vertebrate muscle spindles[2]. Anatomically distinct 'claw' and 'hook' FeCO neurons monitor the position and movement of the tibia, respectively[21,22]. The position-encoding claw neurons are tonically active at different joint angles, whereas the movement-encoding hook neurons are phasic and directionally tuned (Fig. 1b, right). Feedback from FeCO neurons is integrated by circuits in the VNC to control leg posture and movement[23–26]. Previous studies in *Drosophila* have characterized the sensory signals of FeCO neurons during passive (externally imposed) leg movements[21,22]. However, it remains unknown whether FeCO neurons receive presynaptic inhibition during active (self-generated) leg movements, and if so, which circuits mediate this inhibition.

Using cell type-specific calcium imaging in behaving flies, we show that the movement-encoding hook axons, but not the position-encoding claw axons, are suppressed during walking and grooming. Using connectomics, we identify a specific class of GABAergic interneurons that provide most of the inhibitory presynaptic input to the hook axons. These interneurons receive input from multiple descending neurons. Calcium imaging from both interneurons and descending neurons reveals a circuit through which the brain suppresses expected proprioceptive movement feedback during self-generated leg movements.

[1]Department of Neurobiology and Biophysics, University of Washington, Seattle, WA, USA. [2]Department of Biology, University of Washington, Seattle, WA, USA. [3]Present address: Neurobiology and Genetics, Julius-Maximilians-University of Würzburg, Würzburg, Germany. [4]Present address: School of Neuroscience, Virginia Tech, Blacksburg, VA, USA. ✉e-mail: tuthill@uw.edu

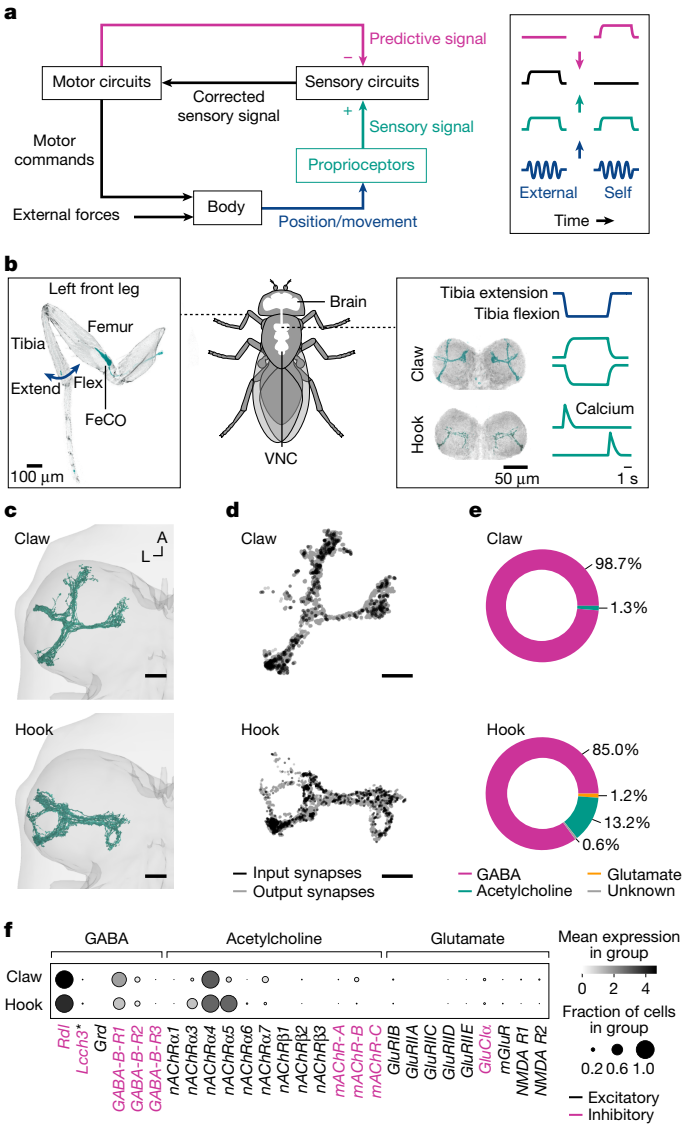

Fig. 1 | Proprioceptor axons from the *Drosophila* leg are positioned to receive presynaptic inhibition. a, Left, theoretical framework for the predictive inhibition of proprioceptive pathways. Right, Schematic time courses illustrating the cancellation of a self-generated proprioceptive signal. **b**, Left, confocal image of a front leg showing the location of the FeCO cell bodies and dendrites. Green, GFP; grey, cuticle autofluorescence. Right, confocal image of position-encoding claw and movement-encoding hook axons in the VNC. Flexion-encoding and extension-encoding hook axons are overlaid. Green, GFP; grey, neuropil stain (nc82). Expression was consistent across animals ($n = 10$). Schematized calcium signals indicate responses to a controlled, passive movement of the femur–tibia joint. **c**, Reconstructed claw ($n = 19$) and hook ($n = 22$) axons in the left front-leg neuromere (FANC connectome). A, anterior; L, left. **d**, Location of postsynaptic (input) and presynaptic (output) synapses of claw and hook axons. View as in **c**. **e**, Neurotransmitter profile of the inputs to claw and hook axons. **f**, Expression levels of receptor genes in claw and hook neurons. Intensity represents the mean level of gene expression; dot size represents the percentage of cells in which gene expression was detected; the asterisk indicates that *Lcch3* forms inhibitory channels with *Rdl* and excitatory channels with *Grd*[60]. In **c** and **d**, scale bars are 20 µm. The fly and leg schematics in **b** are adapted from ref. 26, CC BY 4.0.

Proprioceptor axons receive inhibition

We first examined proprioceptor axons from the fly's left front leg, reconstructed from an electron microscopy volume of a female *Drosophila* VNC (FANC[7]; Fig. 1c, Supplementary Video 1 and Supplementary Table 2). To determine whether proprioceptors receive presynaptic input, we analysed the location and number of the input and output synapses of FeCO axons. Input synapses were present on all axon branches, spatially intermingled with output synapses (Fig. 1d). We found that the presynaptic partners of claw and hook axons were primarily GABAergic (Fig. 1e). Consistent with this finding, we analysed a single-cell RNA-sequencing dataset[22] and found that all claw and hook neurons strongly express the $GABA_A$ receptor gene *Rdl* (Fig. 1f). Together, these data indicate that claw and hook axons are positioned to receive presynaptic inhibition from GABAergic neurons.

Tools to study proprioception in vivo

To investigate the function of presynaptic inhibition of FeCO axons, we developed a set-up for two-photon calcium imaging of neural activity in the VNC and 3D leg tracking of tethered flies on an air-supported ball, which functioned as an omnidirectional treadmill (Fig. 2a and Methods). This set-up allowed us to record calcium signals in FeCO axons and other neurons in the VNC (Extended Data Fig. 1) with the genetically encoded calcium sensor GCaMP while flies walked, groomed or rested on the treadmill.

To compare the neural recordings with hypotheses about circuit function, we constructed computational models that predicted calcium signals in the neurons of interest on the basis of behaviour (Methods). The models convolved a neuron-specific activation function with a GCaMP kernel to translate time courses of joint kinematics or binary behavioural signals into time courses of calcium signals (Fig. 2b).

For claw and hook neurons, the activation function in each model was based on previous calcium imaging and leg tracking data, in which the femur–tibia joint was moved passively[21] (Extended Data Fig. 2a). As a population, claw neurons encode the position of the femur–tibia joint as a deviation from a joint angle of around 80°. Population activity increases nonlinearly with increasing flexion or extension. By contrast, hook neurons respond transiently to flexion or extension of the femur–tibia joint. Our claw and hook models effectively replicated these characteristic calcium signals during passive leg movements (Extended Data Fig. 2b–g). We then used these models to predict calcium signals in FeCO axons during active leg movements (Fig. 2d). This comparison provided a quantitative means to identify context-dependent inhibition and was particularly useful for interpreting calcium signals in claw axons, in which position sensitivity led to unintuitively weak signals in some movement bouts (Extended Data Fig. 3c).

Position feedback is not suppressed

Equipped with computational models to predict calcium signals during active leg movements, we first investigated whether the axons of the position-encoding claw neurons are suppressed during behaviour. We co-expressed the calcium indicator GCaMP and the structural marker tdTomato (for motion correction) with the same cell-specific genetic driver line[21] that was used to tune the passive computational model, and recorded the population activity of claw axons in behaving flies (Fig. 2c and Supplementary Video 2).

Claw axons were active across behaviours, and the passive model effectively tracked the temporal dynamics of the calcium signal (Fig. 2d). This was reflected in high cross-correlation coefficients between measured and predicted calcium signals across trials and flies ($r = 0.91$; Fig. 2e). Calcium signals were also well predicted when we removed the treadmill and flies moved their legs freely in the air (Extended Data Fig. 3c,d).

The characteristic position encoding of claw axons was particularly clear when resting flies held their front leg at a given femur–tibia angle for an extended period of time. Plotting the median amplitude of the calcium signal against the median femur–tibia joint angle for

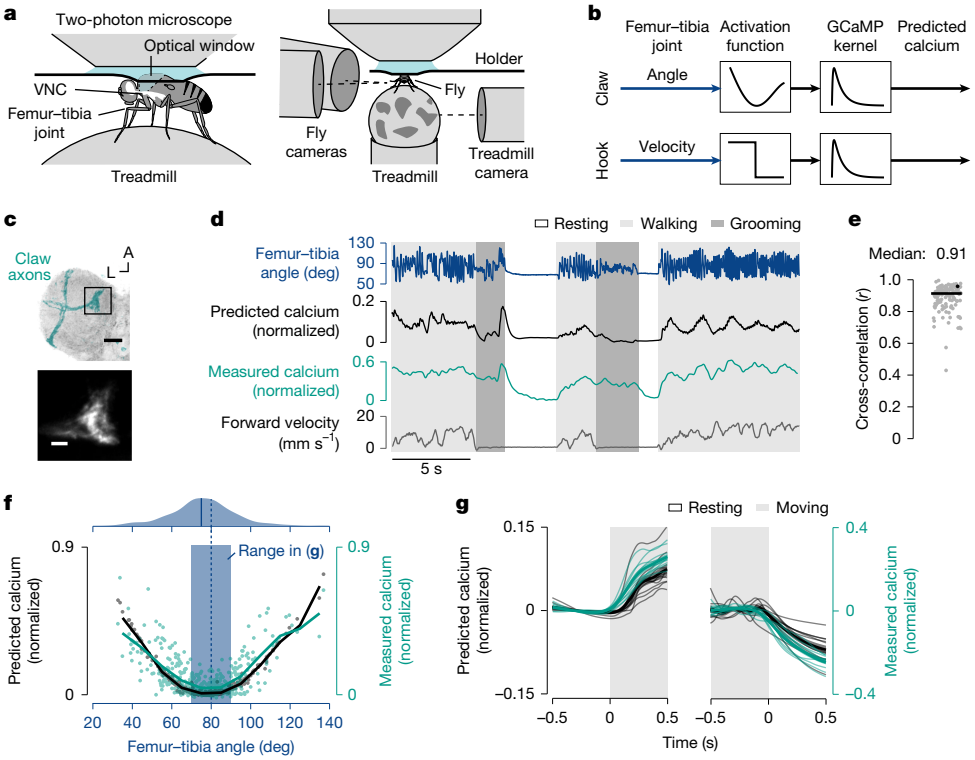

Fig. 2 | The axons of position-encoding proprioceptors are not suppressed during active leg movements. a, Experimental set-up for two-photon calcium imaging from VNC neurons and 3D leg tracking of the left front leg of tethered flies on a treadmill. **b**, Computational models of FeCO proprioceptors that predict calcium signals from femur–tibia joint angles. **c**, Top, confocal image of position-encoding claw axons in the neuromere of the left front leg. Black box, imaging region; green, GFP; grey, neuropil stain (nc82); A, anterior; L, left. Bottom, mean tdTomato signal of a representative trial. Expression was consistent across animals ($n = 11$). Scale bars: top, 20 µm; bottom, 5 µm. **d**, Example of calcium imaging of claw axons during behaviour. **e**, Cross-correlation between predicted and measured calcium signals per trial at a time lag of zero ($n = 11$ flies and 128 trials in total). Black line, median; black dot, trial shown in **d**. **f**, The main graph shows the median predicted and measured calcium signals as a function of the median femur–tibia angle for individual resting bouts ($n = 11$ flies and 480 bouts in total); bouts are at least 1 s in duration. Black and green lines, mean calcium signals in bins of 10°; dashed blue line, resting angle at which activity is minimal; blue rectangle, range of resting angles analysed in **g**. Top, kernel density estimation of the femur–tibia angles during resting. Solid blue line, most frequent femur–tibia angle. **g**, Predicted and measured calcium signals aligned to the transitions into and out of movement; $n = 10$ flies (left), $n = 11$ flies (right). Movement includes walking and grooming. Thin lines, animal means; thick lines, mean of means; shadings, s.e.m.

individual resting bouts (at least 1 s in duration) revealed the expected U-shaped activity pattern centred at around 80° (Fig. 2f, bottom). The minimum signal was close to the most frequent femur–tibia angle that flies adopted when resting on the treadmill (75°; Fig. 2f, top).

Given this U-shaped activity pattern, we expected to see strong changes in the calcium signal when flies transitioned between resting and moving near the most frequent resting angle. Indeed, for transitions towards or away from resting angles of 70° to 90° (Fig. 2f, blue box), calcium signals increased and decreased as predicted by the passive model (Fig. 2g). Notably, the magnitude of the calcium signals tended to be higher than predicted during walking and grooming (Extended Data Fig. 3a,b), which could indicate that claw axons are more sensitive during active movement.

Together, these results indicate that position feedback from claw axons is not suppressed but is transmitted to downstream circuits across behavioural contexts. The close match between the passive claw model predictions and calcium signals recorded during behaviour also provides confidence in our approach of comparing self-generated and passive leg movements in leg proprioceptors.

Movement feedback is suppressed

We next investigated whether the axons of movement-encoding proprioceptors are suppressed during behaviour. We first investigated hook neurons encoding tibia flexion movements. We again co-expressed GCaMP and tdTomato using a cell-specific driver line[21] and recorded the population activity of hook axons in behaving flies (Fig. 3a and Supplementary Video 3).

The passive model predicted strong calcium signals in hook axons during walking and grooming compared with resting (Fig. 3b,d). However, hook calcium signals recorded during behaviour were conspicuously different from these model predictions (Fig. 3b,d). The discrepancy was particularly obvious at the transitions into and out of movement, at which calcium signals did not increase or decrease as predicted (Fig. 3e). Accordingly, the cross-correlation between measured and predicted calcium signals across trials and flies was more variable and lower on average than during passive movement ($r = 0.64$; Fig. 3c, treadmill data). Note that we computed high cross-correlations in some trials simply because those flies did not frequently transition between moving and not moving (Extended Data Fig. 4a). Calcium signals were also absent when we removed the treadmill and flies moved their legs freely in the air (Extended Data Fig. 4c–e). The lack of calcium signals during self-generated movements was even more pronounced in a second driver line[22] for hook flexion neurons (Extended Data Fig. 4f–k). We also observed a similar degree of suppression in hook neurons encoding tibia extension[22] (Extended Data Fig. 5). These results indicate that both flexion-encoding and extension-encoding hook axons are suppressed during self-generated, but not passive, leg movements.

In support of this conclusion, we observed that calcium signals were high when the front leg was moved passively on the treadmill, which sometimes occurred when the front legs stabilized the body during hind-leg grooming (Supplementary Video 3). Calcium signals were also

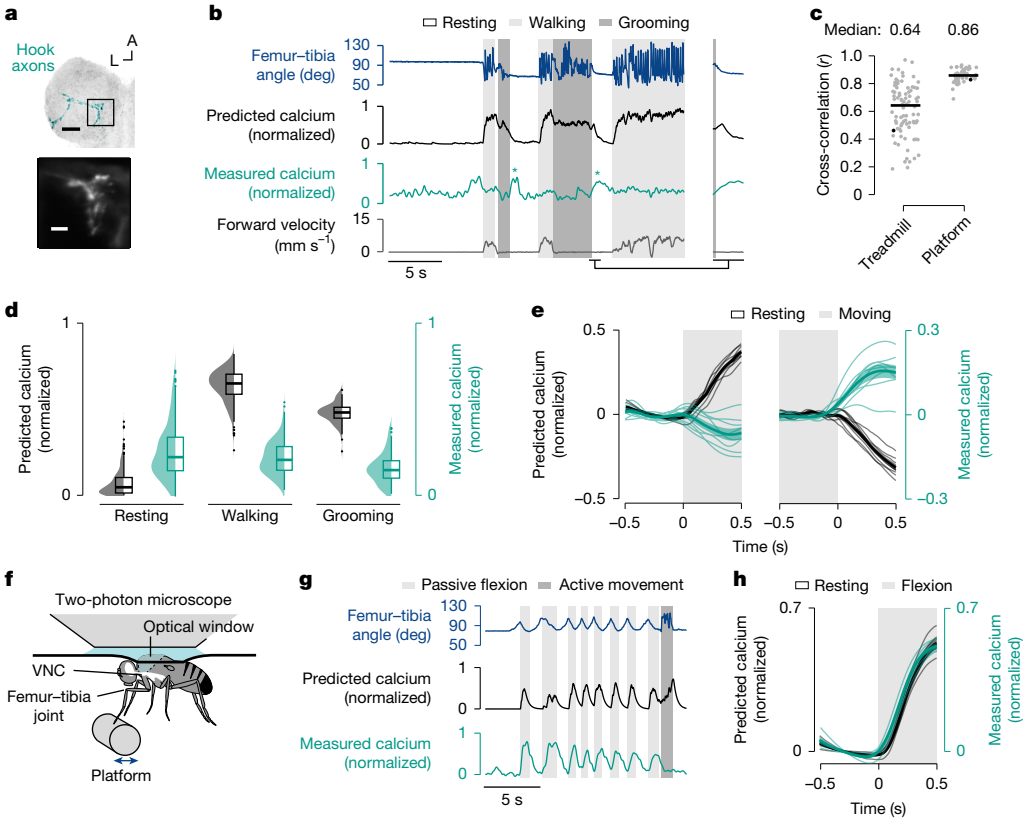

Fig. 3 | The axons of movement-encoding proprioceptors are suppressed during active leg movements. a, Top, confocal image of movement-encoding hook axons in the neuromere of the left front leg. Black box, imaging region; green, GFP; grey, neuropil stain (nc82); A, anterior; L, left. Bottom, mean tdTomato signal of a representative trial. Expression was consistent across animals ($n = 13$). Scale bars: top, 20 µm; bottom, 5 µm. **b**, Example of calcium imaging of hook flexion axons during behaviour. Asterisks highlight resting bouts during which the front leg was held in the air and slowly flexed. **c**, Cross-correlation between predicted and measured calcium signals per trial at a time lag of zero in different movement contexts. Treadmill, $n = 8$ flies and 84 trials; platform, $n = 5$ flies and 47 trials. Black lines, medians; black dots, trials shown in **b** and **g**. In platform trials, active movements were excluded for the cross-correlation. **d**, Median predicted and measured calcium signals during resting ($n = 8$ flies and 237 bouts), walking ($n = 8$ flies and 366 bouts) and grooming ($n = 8$ flies and 93 bouts); bouts are at least 1 s in duration. Distributions, kernel density estimations; boxes, interquartile range (IQR) and median, whiskers extend up to 1.5 × IQR. **e**, Predicted and measured calcium signals aligned to the transitions into and out of movement ($n = 8$ flies). Signals are baseline subtracted (mean from −0.5 to 0 s). Movement includes walking and grooming. Thin lines, animal means; thick lines, mean of means; shadings, s.e.m. **f**, Experimental set-up for passively moving the front leg with a platform during calcium imaging. **g**, Example of calcium imaging of hook flexion axons during behaviour on the platform. **h**, Predicted and measured calcium signals aligned to the transition into passive flexion of the tibia ($n = 5$ flies).

high during resting when the front leg slowly flexed, which we observed after front-leg grooming when the leg was not on the treadmill (Fig. 3b, asterisks) or in trials in which the treadmill was removed (Extended Data Fig. 4c). This response would be predicted by the computational model if leg tracking was noise-free (Extended Data Fig. 2h and Methods). The slow flexions were probably the result of passive forces produced by leg muscles[27] and exoskeletal structures[28].

To further test the idea that hook axons are not suppressed during passive movements, we replaced the treadmill with a moveable platform that flies gripped with the tips of their legs (Fig. 3f). We used the platform to passively move the front leg while imaging from hook axons in the VNC. In this context, we measured strong calcium signals in response to passive movement of the femur–tibia joint, as predicted by the passive model (Fig. 3g,h). This was reflected in higher and less variable cross-correlation coefficients between predicted and measured calcium signals across trials and flies ($r = 0.86$; Fig. 3c, platform data). Because the flies were not anaesthetized, they sometimes actively moved their legs instead of gripping the platform. In line with our previous findings, calcium signals were weak during these active movements (Fig. 3g and Extended Data Fig. 4b).

Finally, we investigated whether differences between the passive model predictions and recorded calcium signals could be due to differences in joint movement dynamics between the active and passive movement conditions. Specifically, flies tended to move their legs more rapidly when they were actively moving than when we moved them during passive stimulation with the platform. Using the same magnetic control system in which we previously investigated proprioceptor responses to passive movements[21,22], we replayed naturalistic time courses of femur–tibia joint angles measured during walking and grooming to otherwise passive animals (Extended Data Fig. 6a,b and Methods). Calcium signals recorded from hook axons in this passive context matched the predictions of the passive model, with calcium signals increasing at the onset of movement, as predicted (Extended Data Fig. 6c–h). Thus, the discrepancy between activity recorded during self-generated movements and the passive model predictions is unlikely to be caused by differences in stimulus statistics.

Together, these results indicate that movement-encoding hook axons are suppressed whenever flies move their legs actively, regardless of the specific movement context.

As well as claw and hook neurons, the FeCO contains a third class of neurons called 'club' neurons, which encode low-amplitude, high-frequency vibrations[21,22]. Club neurons do not feed directly into leg motor circuits[26] and are thought to function as exteroceptors that encode external substrate vibrations[23,24]. We used a cell-specific driver line[22] to record calcium activity in club axons and found that they are not suppressed during active leg movements, similar to claw axons

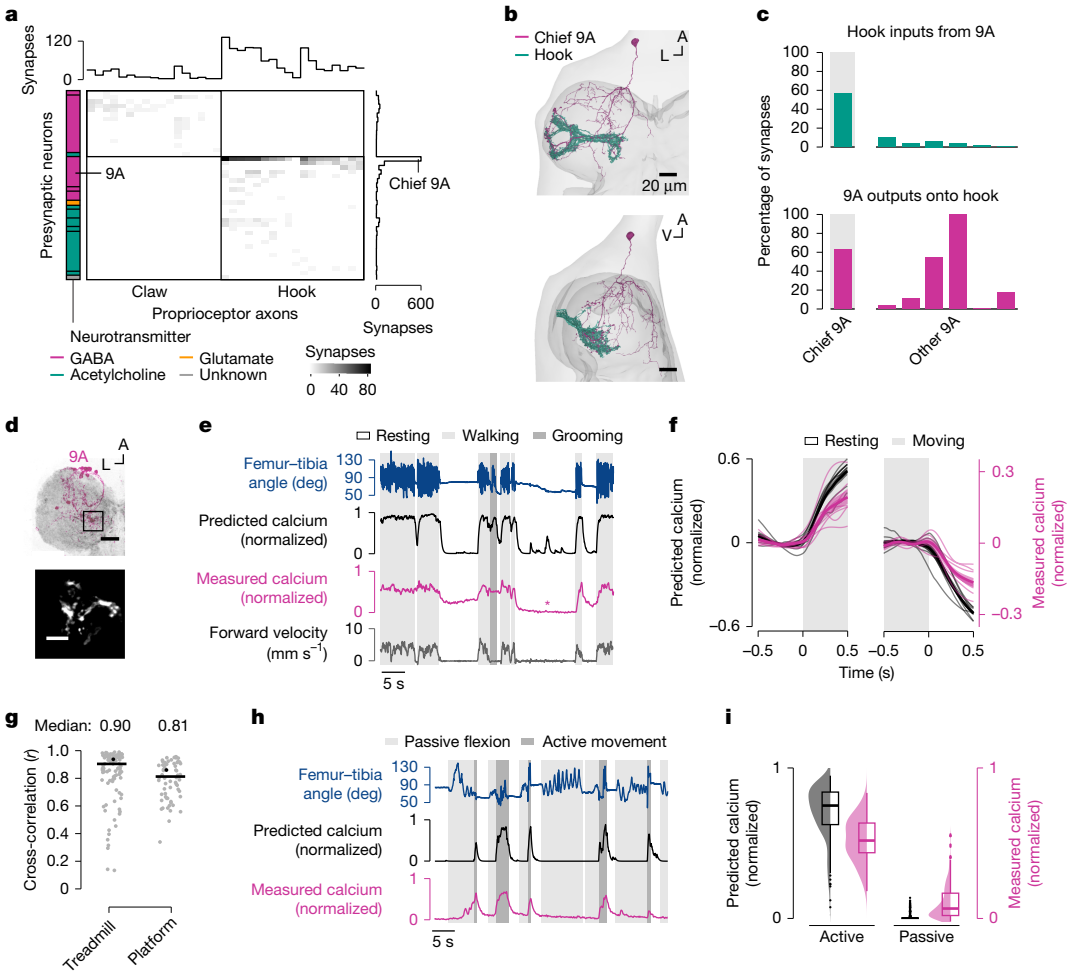

Fig. 4 | GABAergic interneurons provide presynaptic inhibition to movement-encoding proprioceptor axons. a, Connectivity of presynaptic neurons with claw and hook axons. Coloured boxes on the left group presynaptic neurons of the same developmental hemilineage (top to bottom): 13B, 19A, 3A, 9A, 13B, 19A, 8A, 1A, 8B, 18B, 22A, hook axons, hair plate axon, unknown. **b**, Chief 9A neuron in the left front-leg neuromere (FANC connectome). A, anterior; L, left; V, ventral. **c**, Connectivity between 9A neurons and hook axons. **d**, Top, confocal image of 9A neurons in the neuromere of the left front leg. Black box, imaging region; magenta, GFP; grey, neuropil stain (nc82); A, anterior; L, left. Bottom, mean tdTomato signal of a representative trial. Expression was consistent across animals ($n = 10$). Scale bars: top, 20 µm; bottom, 10 µm. **e**, Example of calcium imaging of 9A neurons during behaviour. The asterisk highlights a resting bout during which the front leg was moved passively by the grooming hind legs. **f**, Predicted and measured calcium signals aligned to the transitions into and out of movement ($n = 8$ flies). Movement includes walking and grooming. Thin lines, animal means; thick lines, mean of means; shadings, s.e.m. **g**, Cross-correlation between predicted and measured calcium signals per trial at a time lag of zero in different movement contexts. Treadmill, $n = 8$ flies and 96 trials; platform, $n = 7$ flies and 65 trials. Black lines, medians; black dots, trials shown in **e** and **h**. **h**, Example of calcium imaging of 9A neurons during behaviour on the platform. **i**, Median predicted and measured calcium signals during active ($n = 7$ flies and 159 bouts) and passive ($n = 7$ flies and 399 bouts) movement bouts; bouts are at least 1 s in duration. Distributions, kernel density estimations; boxes, IQR and median, whiskers extend up to 1.5 × IQR.

(Extended Data Fig. 7 and Supplementary Video 4). The baseline activity in club axons was elevated when the legs made contact with the treadmill (Extended Data Fig. 7i,j), consistent with the idea that the neurons function as exteroceptors that detect substrate vibrations.

The 9A neurons provide presynaptic inhibition

To explore the circuit mechanisms underlying the selective suppression of hook axons, we analysed the presynaptic connectivity of claw and hook axons in the female VNC connectome (Fig. 4a). Claw and hook axons receive synaptic input mainly from interneurons in the VNC (claw, 100%; hook: 95%), but not from descending neurons. On average, hook axons receive more presynaptic input than claw axons do (Fig. 4a, top), with most input coming from GABAergic interneurons (Fig. 4a, left). Presynaptic neurons target either claw axons or hook axons, but not both. This could explain why activity was selectively suppressed in hook axons but not in claw axons. Most GABAergic input onto hook axons (83%) comes from a group of local interneurons belonging to the 9A hemilineage[29,30]. One 9A neuron in particular provides 57% of presynaptic input to hook axons (Fig. 4a, right). This chief 9A neuron receives dendritic input in the dorsal VNC and provides synaptic output to hook axons in the ventral VNC (Fig. 4b and Supplementary Video 1). Indeed, most of the output of this chief 9A neuron (63%) is onto hook axons (Fig. 4c). Other 9A neurons also provide much of their output to hook axons (Fig. 4c). Thus, this group of interneurons is positioned to suppress activity selectively in hook axons during active leg movements through presynaptic inhibition.

If these 9A neurons suppress activity in hook axons, we would expect their activity to be high during active leg movements and low during passive leg movements; this is the opposite activity pattern to that observed in hook axons. We instantiated this prediction in a simple computational model, in which calcium activity is high during active flexion and extension movements, but not during resting or passive leg movements (Extended Data Fig. 2a and Methods). We then tested

the predictions of the model by recording the population activity of 9A axons in a region near the terminals of hook axons in the front-leg neuromere using a cell-specific genetic driver line (Fig. 4d and Supplementary Video 5). As predicted, we measured strong calcium signals in the axons of the 9A neurons during walking and grooming (Fig. 4e), with calcium signals increasing and decreasing at the transitions into and out of movement, respectively (Fig. 4f). This was reflected in high cross-correlation coefficients between predicted and measured calcium signals across trials and flies ($r = 0.90$; Fig. 4g, treadmill data). Calcium signals were also well predicted when we removed the treadmill and flies moved their legs freely in the air ($r = 0.95$; Extended Data Fig. 8a–c). Notably, calcium signals in 9A neurons were weak when the front leg was at rest when the other legs moved actively, as was the case during hind-leg grooming (Extended Data Fig. 8d). This indicates that 9A neurons can be recruited in a leg-specific manner.

Calcium signals in 9A neurons were also weak when the grooming hind legs passively moved the front leg (Fig. 4e, asterisk, and Supplementary Video 5). To further test whether calcium signals in 9A axons are absent during passive leg movements, we again used the platform set-up to passively move the femur–tibia joint (Fig. 4h). Because flies were not anaesthetized, they sometimes actively moved their legs instead of gripping the platform. As predicted by the computational model, calcium signals were weak during passive leg movements and strong during active leg movements (Fig. 4g–i).

Together, these results demonstrate that local GABAergic 9A neurons are active during self-generated, but not passive, leg movements. The synaptic connectivity and activity pattern of these neurons indicate that they selectively suppress hook axons by presynaptic inhibition.

Owing to the distributed structure of leg sensorimotor circuits[31], the behavioural function of presynaptic inhibition is challenging to test. Leg-specific optogenetic silencing of 9A neurons in tethered walking flies did not affect leg kinematics (Extended Data Fig. 8f–i and Methods), indicating that the motor circuits are robust to perturbation of specific feedback channels (Supplementary Discussion).

The 9A neurons receive descending input

To explore the origins of context-dependent activity in GABAergic 9A neurons, we analysed their presynaptic inputs in the connectome (Fig. 5a). The 9A neurons receive little direct input from sensory neurons, indicating that they are not driven by sensory feedback from the leg. The chief 9A neuron, which provides most of the input to hook axons, receives most of its input from descending neurons (68%; Fig. 5a). The other 9A neurons receive most of their input from local premotor neurons in the VNC, but some neurons of the group also receive substantial descending input (Fig. 5a).

Some of the descending neurons presynaptic to chief 9A target only the neuromere of the left front leg (Fig. 5b, left), in line with our observation that 9A neurons can be controlled in a leg-specific manner. Most of the descending neurons target multiple leg neuromeres (Fig. 5b, middle). This raised the possibility that the circuit motif we identified for the left front leg is present for all the legs. To test this possibility, we turned to a second VNC connectome of a male fly that is more fully reconstructed in the middle and rear neuromeres (MANC[8,9]; Methods). In support of our hypothesis, we found that hook axons in all leg neuromeres in the male connectome receive most of their input from a 9A neuron resembling the chief 9A neuron in the female connectome (Extended Data Fig. 9a). These chief 9A neurons target mostly hook axons (58% of output synapses) and provide little output to other sensory axons (13%; Extended Data Fig. 9c). Moreover, the top descending neurons presynaptic to the chief 9A neurons resemble those in the female connectome (Extended Data Fig. 9a,b). Thus, the inhibitory circuit motif is present in both females and males, and is segmentally repeated to inhibit hook axons from all legs.

To better understand the logic of the descending control of 9A neurons, we grouped the descending neurons on the basis of their predicted neurotransmitter (Fig. 5c and Methods). We found that the descending input to 9A neurons is mostly cholinergic (excitatory; Fig. 5c and Extended Data Fig. 9d,e). Strikingly, some of the cholinergic descending neurons are known to drive walking[32–34] (DNg100 (BDN2), DNg97 (oDN1), DNg75 (cDN1) and DNa02) and front-leg grooming[35] (DNg12). Together, the walking and grooming descending neurons provide 31% of the synaptic input to the chief 9A neuron (18% and 13%, respectively), and they also target other 9A neurons (Fig. 5b and Extended Data Fig. 9d,e). This indicates that parallel excitatory descending pathways can recruit the 9A neurons to drive feedback inhibition during walking and grooming, while also acting on motor circuits in the VNC. To test whether the descending pathways are capable of driving the inhibition of hook axons, we optogenetically activated one pair of descending neurons (DNg100)[32] while imaging hook flexion axons in the VNC during passive leg movements (Extended Data Fig. 10a–e and Methods). After the end of the optogenetic activation, calcium signals in the hook axons increased, indicating a release from inhibition (Supplementary Discussion).

The 9A neurons also receive inhibitory descending input (Fig. 5c and Extended Data Fig. 9d,e). The neuron providing the most inhibitory input is the GABAergic DNg74 ('web' neuron)[36], which primarily targets the leg neuropils[37] (Fig. 5b,d). We found that, in the VNC, DNg74 targets mostly interneurons (80% of output synapses), including the chief 9A neurons (2%; Extended Data Fig. 9f). To explore which brain regions provide input to DNg74, we turned to a brain connectome of a female fly (FAFB/FlyWire[38–40]; Methods). We found that DNg74 receives input from neurons central to the brain (59 neurons, 48% of input synapses), ascending neurons (74 neurons, 27%) and descending neurons (37 neurons, 25%; Extended Data Fig. 9g). Most of the brain input (61%) comes from the gnathal ganglia, a brainstem-like region important for descending locomotor control[41].

If DNg74 helps to control the 9A neurons, we would expect its activity to be low during active leg movements (corresponding to disinhibition) and high during passive leg movements or resting; this is the opposite activity pattern to that observed in the 9A neurons. We instantiated this prediction in a simple computational model in which calcium activity is high during resting but low during active leg movements (Methods). We then tested the predictions of the model by recording from DNg74 in the front-leg neuromere using a cell-specific driver line[37] (Fig. 5e and Supplementary Video 6). As predicted, we measured strong calcium signals during resting, but not during walking (Fig. 5f), with calcium signals decreasing and increasing at the transitions into and out of movement, respectively (Fig. 5g). This was reflected in high cross-correlation coefficients between predicted and measured calcium signals across trials and flies ($r = 0.94$; Fig. 5h). Calcium signals were also weak when we removed the treadmill and flies moved their legs freely in the air (Extended Data Fig. 10f). Notably, calcium signals in DNg74 were also weak when the front leg was at rest while the other legs moved actively, as was the case during hind-leg grooming (Fig. 5f, asterisk and right). This indicates that the GABAergic DNg74 disinhibit their postsynaptic target neurons throughout the VNC during self-generated leg movements.

To explore the interactions between the excitatory and inhibitory descending inputs to chief 9A neurons, we simulated neural activity in the VNC using a connectome-constrained computational model[42] (Fig. 5i and Methods). The model treats each neuron in the connectome as a leaky integrate-and-fire unit that has an excitatory or inhibitory effect on its postsynaptic partners, based on the neuron's predicted neurotransmitter and number of synapses. When we stimulated the excitatory walking (DNg100) or front-leg grooming (DNg12) descending neurons in the model, the chief 9A neurons were reliably recruited in all leg neuromeres or the front-leg neuromere, respectively (Fig. 5i). However, when we co-activated the inhibitory DNg74 neurons, the

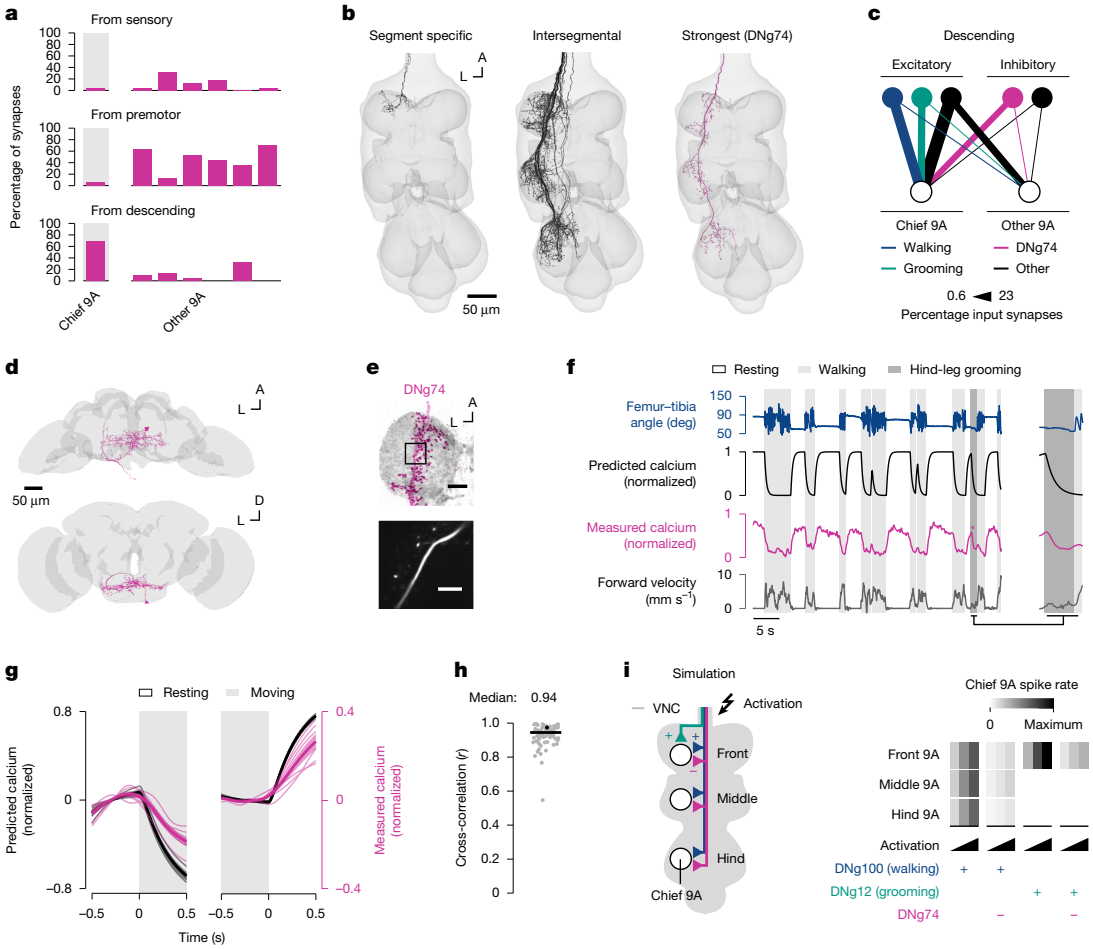

Fig. 5 | GABAergic interneurons receive descending input from the brain. **a**, Connectivity of sensory, premotor and descending neurons with 9A neurons in the front-leg neuromere. **b**, Descending neurons presynaptic to chief 9A (FANC connectome). A, anterior; L, left. **c**, Connectivity between descending neurons and 9A neurons. Nodes represent individual neurons (chief 9A and DNg74) or groups of neurons; lines represent percentage input synapses. The 'walking' node contains DNg100, DNg97, DNg75 and DNa02; the 'grooming' node contains multiple DNg12 neurons. **d**, DNg74 in the brain (FlyWire connectome). A, anterior; D, dorsal; L, left. **e**, Top, confocal image of DNg74 in the neuromere of the left front leg. Black box, imaging region; magenta, GFP; grey, neuropil stain (nc82); A, anterior; L, left. Bottom, mean tdTomato signal of a representative trial. Expression was consistent across animals ($n = 6$). Scale bars: top, 20 µm; bottom, 10 µm. **f**, Example of calcium imaging of DNg74 during behaviour on the treadmill. The asterisk highlights part of a front-leg resting bout during which the hind legs were grooming. **g**, Predicted and measured calcium signals aligned to the transitions into and out of movement ($n = 6$ flies). Movement includes walking and grooming. Thin lines, animal means; thick lines, mean of means; shadings, s.e.m. **h**, Cross-correlation between predicted and measured calcium signals per trial at a time lag of zero ($n = 6$ flies and 74 trials). Black line, median; black dot, trial shown in **f**. **i**, Connectome-constrained computational model simulating recruitment of chief 9A neurons in the left front, middle and hind-leg neuromeres in response to activating descending neurons at different intensities (50 Hz, 150 Hz and 150 Hz).

activity of the chief 9A neurons was strongly reduced. This indicates that control of presynaptic inhibition onto hook axons relies on coordination of the excitatory and inhibitory descending pathways.

Together, these results support a circuit motif in which parallel excitatory and inhibitory descending pathways from motor circuits in the brain control the 9A neurons in a context-dependent manner (Fig. 6a). The motif indicates that during active leg movements, such as walking and grooming, excitatory descending neurons excite the 9A neurons, whereas inhibitory descending neurons release them from inhibition (Fig. 6b, left). During passive leg movements or resting, 9A neurons are not recruited, because of the missing excitatory drive and the inhibition by descending neurons (Fig. 6b, right). The identified excitatory descending neurons that drive walking are intersegmental; they are positioned to recruit 9A neurons in all leg neuromeres (Fig. 6c, left). The excitatory descending neurons that drive front-leg grooming are segment specific; they are positioned to recruit 9A neurons for the front legs, leaving proprioceptive transmission in the standing middle and hind legs unaffected (Fig. 6c, right).

Discussion

In this study, we examine a neural circuit that selectively suppresses proprioceptive feedback from the *Drosophila* leg in a context-dependent manner. Previous studies have shown that proprioceptive pathways can be modulated by inhibition during self-generated limb movements[4–6], but how specific pathways are inhibited during behaviour, as well as the organization and recruitment of the underlying neural circuits, remained unknown. We leveraged connectomics and neural recordings in behaving animals to show that the movement-encoding hook axons, but not the position-encoding claw axons, of the *Drosophila* femoral chordotonal organ are suppressed during self-generated leg movements (Figs. 1–3). The hook axons receive GABAergic presynaptic inhibition from a specific class of interneurons, which are active exclusively during self-generated leg movements (Fig. 4). These neurons receive input from excitatory and inhibitory descending neurons in the brain, and the activity of these descending neurons indicates that they drive feedback inhibition in a predictive manner (Figs. 5 and 6).

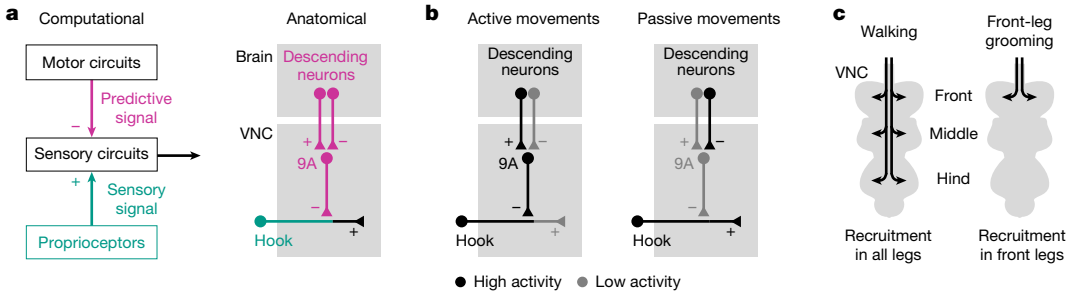

Fig. 6 | Summary of neural circuit for selectively suppressing proprioceptive movement feedback. a, A set of descending neurons target GABAergic 9A neurons in the VNC, which suppress feedback from movement-encoding hook axons by presynaptic inhibition during active, self-generated leg movements. **b**, Context-dependent operation of the circuit motif during active leg movements and passive leg movements or resting. **c**, Recruitment of 9A neurons in different VNC neuropils by excitatory descending neurons that drive walking and front-leg grooming.

Presynaptic inhibition of proprioceptor axons

Our conclusion that hook axons receive GABAergic inhibition is based on three findings: RNA-seq revealed that hook neurons strongly express the $GABA_A$ receptor gene *Rdl*; the connectome revealed GABAergic input onto hook axons; and calcium imaging during behaviour revealed low calcium signals in hook axons and high calcium signals in the presynaptic GABAergic 9A neurons. These findings align with previous electrophysiological recordings demonstrating presynaptic inhibition at FeCO axons in larger insects[4,43–46] and proprioceptive axons in other animals[5,6,18]. The canonical mechanism underlying presynaptic inhibition is that GABA opens chloride channels on the sensory axon by means of $GABA_A$ receptors, causing an efflux of chloride and a membrane depolarization (primary afferent depolarization), shunting of action potentials, and reduced neurotransmitter release[18]. In the future, faster recording techniques such as voltage imaging might reveal whether presynaptic inhibition occurs at specific phases of the step cycle[4] and matches the proprioceptive signal in both timing and magnitude (Supplementary Discussion).

We found that claw axons also receive GABAergic inputs, yet they faithfully signalled joint position across behavioural contexts. Most of this GABAergic input comes from 19A neurons, which receive input from proprioceptive neurons and in turn target proprioceptive axons[9]. The function of GABAergic input onto claw axons remains to be determined, but on the basis of studies in other animals, we speculate that it could sharpen receptive fields through lateral inhibition, protect the sensory terminals from habituation, or reduce hysteresis in postsynaptic neurons[18]. Calcium signals in claw axons tended to be larger than predicted during active movement, which could indicate that claw neurons are more sensitive during active movement. Our connectome analysis revealed little excitatory input onto claw axons, but claw signals could be amplified by neuromodulators such as octopamine, as has been shown specifically for position-encoding FeCO neurons of larger insects[47,48].

Selective inhibition of movement feedback

From a control perspective, selective suppression of movement feedback by presynaptic inhibition could increase the animal's sensitivity to external perturbations and facilitate compensatory motor actions. Movement feedback might be particularly suited for this task because perturbations can be detected more rapidly than by position feedback[2]. By contrast, transmission of position feedback across behaviours allows for postural reflexes at rest[49] and online corrections of leg position in space when moving[50–52]. To support both functions, context-dependent modulation of sensory feedback would have to occur at the level of interneurons, rather than sensory axons. This is seen in the vestibular system of primates, in which sensory axons faithfully relay head motion information regardless of the behavioural context, and context-dependent modulation occurs at the level of interneurons[53]. In the future, it will be interesting to test whether the logic of selective suppression of proprioceptive axons extends to analogous position-encoding (type II muscle spindle afferents) and movement-encoding (type Ia muscle spindle afferents) proprioceptors in mammals.

Predictive inhibition from the brain

We found that the GABAergic 9A neurons are exclusively active during self-generated but not passive leg movements, and that they receive synaptic input mainly from descending neurons (chief 9A) or premotor neurons in the VNC (other 9A). Although we cannot completely rule out sensory feedback having a role, these findings strongly indicate that 9A-mediated inhibition precedes the onset of movement. This is in line with previous work showing that predictive inhibition can originate in motor circuits in the brain[54–58] or nerve cord[59].

Our finding that chief 9A neurons receive most of their input from descending neurons indicates that presynaptic inhibition of hook proprioceptors is driven mainly by the brain. Our connectome analysis showed that the same excitatory descending neurons that drive movement (such as DNg100 and DNg12) or inhibitory descending neurons that are active during rest (DNg74, for example) are also positioned to control the activity of 9A neurons presynaptic to hook axons from specific legs. This circuit organization provides an efficient means to predictively inhibit leg proprioceptors in a context-specific and leg-specific manner.

Online content

Any methods, additional references, Nature Portfolio reporting summaries, source data, extended data, supplementary information, acknowledgements, peer review information; details of author contributions and competing interests; and statements of data and code availability are available at https://doi.org/10.1038/s41586-025-09554-2.

1. Proske, U. & Gandevia, S. C. The proprioceptive senses: their roles in signaling body shape, body position and movement, and muscle force. *Physiol. Rev.* **92**, 1651–1697 (2012).
2. Tuthill, J. C. & Azim, E. Proprioception. *Curr. Biol.* **28**, R194–R203 (2018).
3. Azim, E. & Seki, K. Gain control in the sensorimotor system. *Curr. Opin. Physiol.* **8**, 177–187 (2019).
4. Wolf, H. & Burrows, M. Proprioceptive sensory neurons of a locust leg receive rhythmic presynaptic inhibition during walking. *J. Neurosci.* **15**, 5623–5636 (1995).
5. Fink, A. J. P. et al. Presynaptic inhibition of spinal sensory feedback ensures smooth movement. *Nature* **509**, 43–48 (2014).
6. Koch, S. C. et al. RORβ spinal interneurons gate sensory transmission during locomotion to secure a fluid walking gait. *Neuron* **96**, 1419–1431 (2017).
7. Azevedo, A. et al. Connectomic reconstruction of a female *Drosophila* ventral nerve cord. *Nature* **631**, 360–368 (2024).

8. Takemura, S. et al. A connectome of the male *Drosophila* ventral nerve cord. *eLife* **13**, RP97769 (2024).
9. Marin, E. C. et al. Systematic annotation of a complete adult male *Drosophila* nerve cord connectome reveals principles of functional organisation. *eLife* **13**, RP97766 (2024).
10. Rossignol, S., Dubuc, R. & Gossard, J.-P. Dynamic sensorimotor interactions in locomotion. *Physiol. Rev.* **86**, 89–154 (2006).
11. Dallmann, C. J., Karashchuk, P., Brunton, B. W. & Tuthill, J. C. A leg to stand on: computational models of proprioception. *Curr. Opin. Physiol.* **22**, 100426 (2021).
12. Frigon, A., Akay, T. & Prilutsky, B. I. Control of mammalian locomotion by somatosensory feedback *Compr. Physiol.* **12**, 2877–2947 (2021).
13. McComas, A. J. Hypothesis: Hughlings Jackson and presynaptic inhibition: is there a big picture? *J. Neurophysiol.* **116**, 41–50 (2016).
14. Crapse, T. B. & Sommer, M. A. Corollary discharge across the animal kingdom. *Nat. Rev. Neurosci.* **9**, 587–600 (2008).
15. Straka, H., Simmers, J. & Chagnaud, B. P. A new perspective on predictive motor signaling. *Curr. Biol.* **28**, R232–R243 (2018).
16. Cullen, K. E. Sensory signals during active versus passive movement. *Curr. Opin. Neurobiol.* **14**, 698–706 (2004).
17. Daly, K. C. & Dacks, A. The self as part of the sensory ecology: how behavior affects sensation from the inside out. *Curr. Opin. Insect Sci.* **58**, 101053 (2023).
18. Clarac, F. & Cattaert, D. Invertebrate presynaptic inhibition and motor control. *Exp. Brain Res.* **112**, 163–180 (1996).
19. Rudomin, P. & Schmidt, R. F. Presynaptic inhibition in the vertebrate spinal cord revisited. *Exp. Brain Res.* **129**, 1–37 (1999).
20. Kuan, A. T. et al. Dense neuronal reconstruction through X-ray holographic nano-tomography. *Nat. Neurosci.* **23**, 1637–1643 (2020).
21. Mamiya, A., Gurung, P. & Tuthill, J. C. Neural coding of leg proprioception in *Drosophila*. *Neuron* **100**, 636–650 (2018).
22. Mamiya, A. et al. Biomechanical origins of proprioceptor feature selectivity and topographic maps in the *Drosophila* leg. *Neuron* **111**, 3230–3243 (2023).
23. Agrawal, S. et al. Central processing of leg proprioception in *Drosophila*. *eLife* **9**, e60299 (2020).
24. Chen, C. et al. Functional architecture of neural circuits for leg proprioception in *Drosophila*. *Curr. Biol.* **31**, 5163–5175 (2021).
25. Chockley, A. S. et al. Subsets of leg proprioceptors influence leg kinematics but not interleg coordination in *Drosophila melanogaster* walking. *J. Exp. Biol.* **225**, jeb244245 (2022).
26. Lee, S.-Y. J., Dallmann, C. J., Cook, A., Tuthill, J. C. & Agrawal, S. Divergent neural circuits for proprioceptive and exteroceptive sensing of the *Drosophila* leg. *Nat. Commun.* **16**, 4105 (2025).
27. Hooper, S. L. et al. Neural control of unloaded leg posture and of leg swing in stick insect, cockroach, and mouse differs from that in larger animals. *J. Neurosci.* **29**, 4109–4119 (2009).
28. Ache, J. M. & Matheson, T. Passive joint forces are tuned to limb use in insects and drive movements without motor activity. *Curr. Biol.* **23**, 1418–1426 (2013).
29. Harris, R. M., Pfeiffer, B. D., Rubin, G. M. & Truman, J. W. Neuron hemilineages provide the functional ground plan for the *Drosophila* ventral nervous system. *eLife* **4**, e04493 (2015).
30. Lacin, H. et al. Neurotransmitter identity is acquired in a lineage-restricted manner in the *Drosophila* CNS. *eLife* **8**, e43701 (2019).
31. Tuthill, J. C. & Wilson, R. I. Mechanosensation and adaptive motor control in insects. *Curr. Biol.* **26**, R1022–R1038 (2016).
32. Sapkal, N. et al. Neural circuit mechanisms underlying context-specific halting in *Drosophila*. *Nature* **634**, 191–200 (2024).
33. Yang, H. H. et al. Fine-grained descending control of steering in walking *Drosophila*. *Cell* **187**, 6290–6308 (2024).
34. Rayshubskiy, A. et al. Neural circuit mechanisms for steering control in walking *Drosophila*. *eLife* **13**, RP102230 (2025).
35. Guo, L., Zhang, N. & Simpson, J. H. Descending neurons coordinate anterior grooming behavior in *Drosophila*. *Curr. Biol.* **32**, 823–833 (2022).
36. Cheong, H. S. J. et al. Transforming descending input into behavior: the organization of premotor circuits in the *Drosophila* male adult nerve cord connectome. *eLife* **13**, RP96084 (2024).
37. Sterne, G. R., Otsuna, H., Dickson, B. J. & Scott, K. Classification and genetic targeting of cell types in the primary taste and premotor center of the adult *Drosophila* brain. *eLife* **10**, e71679 (2021).
38. Zheng, Z. et al. A complete electron microscopy volume of the brain of adult *Drosophila melanogaster*. *Cell* **174**, 730–743 (2018).
39. Dorkenwald, S. et al. Neuronal wiring diagram of an adult brain. *Nature* **634**, 124–138 (2024).
40. Schlegel, P. et al. Whole-brain annotation and multi-connectome cell typing of *Drosophila*. *Nature* **634**, 139–152 (2024).
41. Emanuel, S., Kaiser, M., Pflueger, H.-J. & Libersat, F. On the role of the head ganglia in posture and walking in insects. *Front. Physiol.* **11**, 135 (2020).
42. Shiu, P. K. et al. A *Drosophila* computational brain model reveals sensorimotor processing. *Nature* **634**, 210–219 (2024).
43. Burrows, M. & Laurent, G. Synaptic potentials in the central terminals of locust proprioceptive afferents generated by other afferents from the same sense organ. *J. Neurosci.* **13**, 808–819 (1993).
44. Burrows, M. & Matheson, T. A presynaptic gain control mechanism among sensory neurons of a locust leg proprioceptor. *J. Neurosci.* **14**, 272–282 (1994).
45. Sauer, A. E., Büschges, A. & Stein, W. Role of presynaptic inputs to proprioceptive afferents in tuning sensorimotor pathways of an insect joint control network. *J. Neurobiol.* **32**, 359–376 (1997).
46. Gebehart, C. & Büschges, A. The processing of proprioceptive signals in distributed networks: insights from insect motor control. *J. Exp. Biol.* **227**, jeb246182 (2024).
47. Ramirez, J.-M., Büschges, A. & Kittmann, R. Octopaminergic modulation of the femoral chordotonal organ in the stick insect. *J. Comp. Physiol. A* **173**, 209–219 (1993).
48. Matheson, T. Octopamine modulates the responses and presynaptic inhibition of proprioceptive sensory neurones in the locust *Schistocerca gregaria*. *J. Exp. Biol.* **200**, 1317–1325 (1997).
49. Bässler, U. The femur-tibia control system of stick insects: a model system for the study of the neural basis of joint control. *Brain Res. Rev.* **18**, 207–226 (1993).
50. Dean, J. Control of leg protraction in the stick insect: a targeted movement showing compensation for externally applied forces. *J. Comp. Physiol. A* **155**, 771–781 (1984).
51. Takeoka, A., Vollenweider, I., Courtine, G. & Arber, S. Muscle spindle feedback directs locomotor recovery and circuit reorganization after spinal cord injury. *Cell* **159**, 1626–1639 (2014).
52. Mayer, W. P. & Akay, T. The role of muscle spindle feedback in the guidance of hindlimb movement by the ipsilateral forelimb during locomotion in mice. *eNeuro* **8**, ENEURO.0432-21.2021 (2021).
53. Mackrous, I., Carriot, J. & Cullen, K. E. Context-independent encoding of passive and active self-motion in vestibular afferent fibers during locomotion in primates. *Nat. Commun.* **13**, 120 (2022).
54. Seki, K., Perlmutter, S. I. & Fetz, E. E. Sensory input to primate spinal cord is presynaptically inhibited during voluntary movement. *Nat. Neurosci.* **6**, 1309–1316 (2003).
55. Tomatsu, S., Kim, G., Kubota, S. & Seki, K. Presynaptic gating of monkey proprioceptive signals for proper motor action. *Nat. Commun.* **14**, 6537 (2023).
56. Pichler, P. & Lagnado, L. Motor behavior selectively inhibits hair cells activated by forward motion in the lateral line of zebrafish. *Curr. Biol.* **30**, 150–157 (2020).
57. Odstrcil, I. et al. Functional and ultrastructural analysis of reafferent mechanosensation in larval zebrafish. *Curr. Biol.* **32**, 176–189 (2022).
58. Wallach, A. & Sawtell, N. B. An internal model for canceling self-generated sensory input in freely behaving electric fish. *Neuron* **111**, 2570–2582 (2023).
59. Poulet, J. F. A. & Hedwig, B. The cellular basis of a corollary discharge. *Science* **311**, 518–522 (2006).
60. Gisselmann, G., Plonka, J., Pusch, H. & Hatt, H. *Drosophila melanogaster* GRD and LCCH3 subunits form heteromultimeric GABA-gated cation channels. *Br. J. Pharmacol.* **142**, 409–413 (2004).

Methods

Experimental animals

We used *D. melanogaster* raised on standard cornmeal and molasses medium at 25 °C in a 14:10-h light:dark cycle. Imaging experiments in behaving animals were performed using males 1–9 days old. Imaging experiments in fully restrained animals without optogenetic activation were performed using females 4–8 days old. Imaging experiments with optogenetic activation were performed using females 10–14 days old that were kept in the dark on cornmeal agar with all-*trans* retinal (35 mM in 95% EtOH; Santa Cruz Biotechnology) for their entire life cycle until the experiment. Optogenetic experiments on the ball were performed using females 2–5 days old kept in the dark on retinal food for 24–72 h before the experiment. The genetic driver lines used for the experiments are shown in Extended Data Fig. 1. The genotypes are listed in Supplementary Table 1.

Immunohistochemistry

The VNC dissections and immunohistochemistry for FeCO axons and 9A neurons were done as in ref. 23. The primary antibodies used were rat anti-CD8 (1:50 concentration) and mouse anti-Bruchpilot (for neuropil staining, 1:50 concentration). The secondary antibodies used were goat anti-rat Alexa Fluor 488 (1:250 concentration) and goat anti-mouse Alexa Fluor 633 (1:250 concentration). Z-stacks of VNCs were acquired using a confocal microscope (Zeiss 510). The expression patterns in the VNC were aligned to a female VNC template[61] in Fiji[62] using the Computational Morphometry Toolkit (Neuroimaging Informatics Tools and Resources Clearinghouse). Confocal stacks of the claw line, one of the hook flexion lines (driver line 1), and the DNg74 line were downloaded from the GAL4 and split-GAL4 collections on FlyLight[63,64].

Analysis of RNA-seq data

The RNA-seq data of FeCO neurons were generated in a previous study[22]. We queried the dataset for the expression of different receptor genes in claw, hook and club neurons using SCope[65].

Two-photon imaging in behaving animals

Preparation. To record calcium signals in the VNC of behaving flies, we adapted a previously described preparation[66,67]. In brief, we clipped the fly's wings under cold anaesthesia and glued the dorsal thorax to a custom-made holder with a 0.8 mm × 0.95 mm opening (KOA 300; Kemxert). To gain optical access to the VNC, we opened the dorsal side of the thorax and removed the indirect flight muscles, the trachea above the neck connective and the underlying fat bodies using forceps, and then pinned the digestive tract to the side. After the dissection, the fly holder was mounted onto a three-axis manipulator, and the fly was positioned on top of the treadmill. We gave flies 30–60 min to recover from the preparation before starting the experiments. All experiments were done in the dark at room temperature.

Set-up. Calcium signals were recorded using a two-photon Movable Objective Microscope (MOM, Sutter Instruments) with a 20× water-immersion objective lens (Olympus XLUMPlanFI, 0.95 NA, 2.0 mm wd; Olympus). Neurons of interest expressed the calcium indicator GCaMP6f or GCaMP7f (green fluorescence) and the structural marker tdTomato (red fluorescence). Fluorophores were excited at 920 nm by a mode-locked Ti:sapphire laser (Chameleon Vision S, Coherent). We used a Pockels cell to keep the power at the back aperture of the objective below about 35 mW. The emitted fluorescence was directed to two high-sensitivity GaAsP photomultiplier tubes (Hamamatsu Photonics) through a 705-nm edge dichroic beamsplitter followed by a 580-nm edge image-splitting dichroic beamsplitter (Semrock). Fluorescence was band-passed filtered by either a 525/50 (green) or 641/75 (red) emission filter (Semrock). Image acquisition was controlled using ScanImage 5.2 (Vidrio Technologies) in Matlab (MathWorks). The microscope was equipped with a galvo-resonant scanner, and the objective lens was mounted onto a piezo actuator (Physik Instrumente; digital piezo controller E-709). We acquired volumes of 3 512 × 512-pixel images spaced 5 µm apart in depth (10 µm in total) at a speed of 8.26 volumes per second. We typically recorded 400 volumes (about 50 s) per trial. Previous experiments revealed that calcium signals in claw and hook axons do not differ qualitatively across different axon branches when the leg is moved passively[21]. We therefore focused our experiments on a single imaging region (indicated in the figures).

Flies were positioned on top of an omnidirectional treadmill consisting of a patterned Styrofoam ball (9.1 mm diameter, 0.12 g) floating on air in an aluminium holder. The air flow was set to about 500 ml min^{-1}. The ball was illuminated by two infrared LEDs (850 nm peak wavelength; ThorLabs). Ball movements were recorded at 30 Hz with a camera (Basler acA1300-200um) equipped with a macro zoom lens (Computar MLM3X-MP; Edmund Optics). Ball rotations around the fly's cardinal body axes (forward, rotational and sideward) were reconstructed offline using FicTrac[68]. Velocities of the fly were calculated on the basis of the known diameter of the ball. Velocities were upsampled to the sampling rate of leg tracking (300 Hz) using cubic spline interpolation and then low-pass filtered using a moving average filter with a time window of 0.2 s.

The platform used to move the leg passively consisted of a metal pin (0.5 mm diameter, 4.4 mm length) mounted onto a three-axis micromanipulator (MP-225; Sutter Instruments). The pin was wrapped in black sandpaper to provide sufficient grip for the flies' tarsi. The micromanipulator was controlled manually.

Movements of the left front leg were recorded at 300 Hz with two cameras (Basler acA800-510um) equipped with 1.0× InfiniStix lenses (68 mm wd; Infinity) and 875-nm short-pass filters (Edmund Optics). The leg was illuminated by an infrared LED (850-nm peak wavelength; ThorLabs). We trained a deep neural network (DeepLabCut[69]) to automatically track all leg joints in each camera view. We combined 2D tracking data from both camera views to reconstruct leg-joint positions and angles in 3D using Anipose[70]. We applied a median filter on the 2D tracking data and then used spatiotemporally regularized triangulation. The two cameras were calibrated using a ChArUco board (6 × 6 markers, 4 bits per marker, 0.125 mm marker length). The 3D leg tracking was necessary to provide accurate femur–tibia joint angle information for the computational models that predicted calcium signals in our neurons of interest.

Two-photon image analysis. Two-photon images were analysed with custom scripts in Matlab. All images were smoothed with a Gaussian filter (σ = 3 pixels, size = 5 × 5 pixels) and then corrected for horizontal movement of the VNC. Each tdTomato image was aligned to the average tdTomato signal of the recorded trial through translations using a cross-correlation-based image-registration algorithm[71] (upsampling factor = 4). The same translations were then applied to the GCaMP images. After horizontal movement correction, the three GCaMP and tdTomato images per volume were averaged and we extracted the mean fluorescence from manually drawn regions of interest. Next, we corrected for vertical movement of the VNC by computing the ratio of GCaMP fluorescence to tdTomato fluorescence in each frame[72]. Dividing the GCaMP fluorescence by the tdTomato fluorescence decreased the impact of vertical movement, because such movements result in correlated changes in both signals, and the tdTomato signal is independent of neural activity. To facilitate comparisons across trials and flies, ratio values were z-scored by subtracting the mean of a baseline ratio and dividing by the standard deviation of that baseline ratio. The baseline was defined in each trial as the 10% smallest ratio values. The z-scored ratio values were upsampled to the sampling rate of leg tracking (300 Hz) using cubic spline interpolation and low-pass filtered using a moving average filter with a time window of 0.2 s. Finally, to enable comparisons with predicted calcium values, we normalized

the measured calcium values to be between 0 and 1 by dividing each *z*-scored ratio value by the maximum *z*-scored ratio value for a given genetic driver line in the dataset. Normalizing all calcium signals in a dataset by the same value enabled us to compare magnitudes across trials. Because the normalization affected the magnitude of the calcium signal equally across trials without changing relative differences between trials, the specific value used for normalization did not affect our conclusions.

Similarly, calcium signals from ref. 21 were first *z*-scored per trial relative to a baseline and then divided by the maximum *z*-scored value for a given genetic driver line in the dataset.

Data annotations and data selection. Fly behaviour was classified semi-automatically on the basis of the leg-tracking data. All classifications were reviewed and manually corrected if necessary. First, movement of the left front leg was determined on the basis of the speed of the leg's tarsus in the side-view camera. The velocity was low-pass filtered using a moving average filter with a time window of 0.3 s. Frames in which the velocity exceeded 0.8 pixels s^{-1} were classified as moving. We then applied a hysteresis filter, which assigned epochs of up to 250 ms to the previous epoch (moving or not moving). In trials involving the treadmill, movements were further classified as walking or grooming, on the basis of the movement of the left middle leg. Movement of the middle leg was determined analogously to that of the front leg. Epochs in which both the front leg and the middle leg moved were classified as walking. Epochs in which the front leg but not the middle leg moved were classified as front-leg grooming. Front-leg movements other than walking or grooming (such as pushing) were manually classified as 'other'.

For trials involving the platform, we manually annotated periods of passive leg movement based on the leg videos. For hook flexion neurons, we annotated passive flexions of the femur–tibia joint (Fig. 3g). For hook extension neurons, we annotated passive extensions of the femur–tibia joint (Extended Data Fig. 5). For 9A neurons, we annotated all passive movements of the leg (Fig. 4h). For DNg74, we annotated hind-leg grooming events for the computational model.

Frames were manually excluded from the analysis if the front leg was involved in movements other than walking or grooming on the treadmill (such as pushing), the femur–tibia joint of the front leg was not tracked correctly or the two-photon image registration failed (for example, if the VNC moved out of the imaging volume). When calculating the cross-correlation for hook axon recordings during passive leg movements with the platform, we also excluded frames in which the leg moved actively. Behavioural bouts and movement transitions were excluded if they were shorter than the desired minimum duration (see figure legends).

For some genotypes, we recorded neural activity using GCaMP6f and GCaMP7f (Supplementary Table 1). We did not observe any differences in the calcium signals and therefore pooled recordings for our analysis.

Two-photon imaging in fully restrained animals

Preparation. To record calcium signals in the VNC of fully restrained flies, we used a previously described preparation[21]. In brief, we clipped the fly's wings under cold anaesthesia and attached the thorax ventral side up to a custom-made holder. All legs except for a front leg were glued (KOA 300; Kemxert). To move the tibia of that leg with the magnet, we attached a small piece of insect pin (around 1 mm in length and 0.1 mm in diameter; Living Systems Instrumentation). To gain optical access to the VNC, the cuticle covering the front-leg neuromeres and underlying fat bodies and larger trachea were removed using forceps. To reduce movement of the VNC, we also removed the digestive tract.

Set-up. For the data shown in Extended Data Fig. 6, we used the microscope for imaging behaving animals described above with a 40× water-immersion objective lens (0.8 NA, 2.0 mm wd; Nikon Instruments). We acquired volumes of 3 256 × 128-pixel images spaced 10 µm apart in depth (20 µm in total) at a speed of 36.7 volumes per second. For the data shown in Extended Data Fig. 10b–e, we used the microscope described in ref. 21. We acquired single-plane 256 × 120-pixel images at a speed of 8.01 images per second.

To control the femur–tibia angle, we used a previously described magnet–motor system[21]. In brief, we moved the pin on the tibia using a rare-earth magnet, the position of which was controlled by a servo motor (SilverMax QCI-X23C-1; QuickSilver Controls) using Matlab. The motor was mounted onto a micromanipulator (MP-225; Sutter Instruments), enabling us to adjust its position so that the magnet moved in a circular trajectory centred at the femur–tibia joint.

For data shown in Extended Data Fig. 6, we imposed movements that were representative of femur–tibia joint angles and velocities recorded during walking and grooming. Each trial started at a femur–tibia angle of around 90°. In walking trials, we replayed 67 movement bouts containing different front-leg walking kinematics; each bout was 2 s in duration. In grooming trials, we replayed 12 movement bouts containing different front-leg grooming kinematics. Bout durations ranged from 0.3 s to 2.0 s. Because movement bouts did not necessarily start or end at a femur–tibia angle of 90°, we added a 0.25-s transition phase before and after each bout, in which the tibia was linearly moved to the start position or back to 90°. The tibia was not moved for 0.5 s between stimuli. Movements of the tibia were recorded at 200 Hz using a camera (Basler acA800-510um; Basler) equipped with a 1.0× InfiniStix lens (94 mm wd; Infinity) and a 900-nm short-pass filter (Edmund Optics). Because the servo motor was placed directly under the fly, we placed the camera to the side and used a prism (Edmund Optics) to capture the view from below. The leg was illuminated by an infrared LED (850-nm peak wavelength; Thorlabs). The coxa–femur, femur–tibia and tibia–tarsus joints were tracked using DeepLabCut. Because the tibia moved in a single plane parallel to the surface of the holder, 2D tracking was sufficient to provide accurate femur–tibia joint-angle information for the computational models.

For the data shown in Extended Data Fig. 10b–e, we slowly moved the tibia from extension to flexion (160° to 40°). Movements of the tibia were recorded as described above, but the tibia was tracked on the basis of image thresholding, as described in ref. 21. We recorded 11 trials per animal. We alternated between control trials (six in total) and experimental trials (five in total). In experimental trials, DNg100 was activated optogenetically for 4.0 ± 0.7 s (mean ± s.d.) using a fibre-coupled LED (625 nm, M625F2, Thorlabs) pointed at the thorax of the fly. Because the optogenetic stimulus had to be strong for DNg100 activation, calcium imaging during the activation was not possible with our set-up. Instead, we manually switched off the photomultiplier tube (PMT) before the optogenetic activation and switched it back on immediately after it. For the PMT control data, we recorded 12 trials per animal without tibia movement or optogenetic activation. In each trial, we turned off the PMT for 4.3 ± 0.5 s.

Two-photon image analysis. Two-photon images were analysed using custom scripts in Matlab. All images were smoothed with a Gaussian filter ($\sigma = 3$ pixels, size = 5 × 5 pixels). Owing to minimal VNC movement in fully restrained animals, horizontal and vertical movement correction was not necessary. Instead, we computed the change in GCaMP or GFP fluorescence relative to a baseline per trial. For each frame, we subtracted the mean baseline fluorescence and divided by the mean baseline fluorescence. The baseline was defined for each trial as the lowest mean fluorescence in a 10-frame window (corresponding to 0.27 s in Extended Data Fig. 6 and 1.25 s in Extended Data Fig. 10b–e).

For the data presented in Extended Data Fig. 6, we extracted the mean fluorescence from manually drawn regions of interest, and relative changes in fluorescence were *z*-scored, upsampled, low-pass filtered and normalized as described above.

For the GCaMP data presented in Extended Data Fig. 10b–d, we identified responses of hook flexion axons from the population response of FeCO axons as described in ref. 21, using correlation-based *k*-means clustering that grouped pixels on the basis of the similarity of their intensity change. For the GFP data in that figure, we extracted the mean fluorescence from manually drawn regions of interest.

Computational models for predicting calcium signals

We constructed computational models to predict the time courses of calcium signals in claw, hook, club, 9A and DNg74 neurons from time courses of femur–tibia joint kinematics or binary behaviour variables. The time courses were fed into a neuron type-specific activation function, which was convolved with a double exponential function to mimic the temporal dynamics of GCaMP:

$$e^{-t/\tau_{\mathrm{off}}} - e^{-t/\tau_{\mathrm{on}}},$$

where e is the exponential function, t is time, τ_{on} is the onset time constant (0.03 s) and τ_{off} is the offset time constant (0.3 s). The time constants were tuned to match the measured calcium signals in claw and hook axons in ref. 21 (Extended Data Fig. 2b,d).

The activation functions for claw, hook and club neurons were based on calcium imaging and leg-tracking data from ref. 21, in which the femur–tibia joint was moved passively using ramp-and-hold stimuli. In that dataset, calcium signals in claw axons were lowest at a joint angle of 90° and increased nonlinearly with increasing flexion or extension. To model this encoding, we first subtracted 90° from the tracked femur–tibia joint angle and then fitted a fourth-order polynomial activation function (convolved with the GCaMP kernel) to the *z*-scored and normalized calcium signals using nonlinear least-squares optimization (lsqcurvefit in Matlab; Extended Data Fig. 2a). In our dataset, calcium signals were weakest at a joint angle of 80°. Thus, we subtracted 80° from the tracked femur–tibia joint angle but used the same activation function. The 10° difference between datasets is probably related to differences in leg tracking, not encoding. Note that the activation function was not fully symmetric, with a weaker response when the joint was fully extended. This could be because claw neurons are less sensitive at these joint angles, or because the genetic driver line does not target the specific claw neurons that normally encode these angles.

Hook neurons were assumed to encode flexion or extension direction[21]. To model this encoding, the joint-angle velocity was fed into a binary step function (Extended Data Fig. 2a). For hook flexion neurons, we used a threshold of −5 deg s^{-1} for the dataset from ref. 21 and −50 deg s^{-1} for our dataset. We chose a different threshold for our dataset to account for a greater amount of tracking noise. As a result, the model did not predict the strong calcium signals measured during slow flexions below −50 deg s^{-1} (Fig. 3b). However, using an artificial joint-angle time course without tracking noise as input to the model confirmed that strong calcium signals would be expected during slow flexions (Extended Data Fig. 2h); ref. 21 did not test hook extension neurons, but based on ref. 22, hook extension neurons have the opposite encoding to hook flexion neurons, which we modelled with a binary step function with a threshold of 50 deg s^{-1} in our dataset.

Club neurons were assumed to encode bidirectional movement (flexion and extension)[21]. To model this encoding, the joint-angle velocity was fed into a rectangular function (Extended Data Fig. 2a). Analogously to the hook neurons, we used a threshold of ±5 deg s^{-1} for the dataset from ref. 21 and ±50 deg s^{-1} for our dataset.

For 9A and DNg74 neurons, no previous calcium imaging data were available to fit activation functions. We therefore designed simple activation functions for these neurons based on our hypotheses about their function in the circuit. That is, we intentionally designed the computational models for 9A and DNg74 neurons to predict the neurons' general activity a priori, not to fully explain the measured calcium dynamics. The close correspondence between predicted and measured calcium signals provides confidence in this approach.

Specifically, 9A neurons were assumed to encode bidirectional movement, which we modelled with the same activation function that we used for club neurons (Extended Data Fig. 2a). However, we assumed that 9A neurons do not respond to passive leg movements. To model this, the joint-angle velocity input was set to zero during passive leg movements.

To model the activity of DNg74, we used a binary vector indicating when all legs were at rest as the activation function. This required manual annotations for legs other than the left front leg (see above).

To enable comparisons with measured calcium values, we normalized the predicted calcium values to be between 0 and 1 by subtracting the minimum predicted value in each trial and dividing by the maximum predicted value for a given genetic driver line in the dataset.

Optogenetic experiments on the treadmill

Preparation. We clipped the flies' wings under cold anaesthesia before experiments to prevent visual obstruction of the legs and thorax. To position the fly above the spherical treadmill, a tungsten wire was glued to the dorsal thorax (KOA 300; Kemxert).

Set-up. The treadmill was the same as the one for the calcium imaging experiments. Ball movements were recorded at 30 Hz with a camera (FMVU-03MTM-CS; Point Grey Research) equipped with a macro zoom lens (Computar MLM3X-MP; Edmund Optics). Ball rotations around the fly's cardinal body axes were reconstructed from live video using FicTrac[68]. We coaxed flies to walk on the treadmill by displaying visual stimuli on a semi-circular green LED display[23,73]. We displayed a single dark bar (30° wide) on a light background, and sinusoidally oscillated the bar at 2.7 Hz across 48.75° about the centre of the fly's visual field. Between trials, the LED panels displayed a fixed dark stripe (30°) on a bright background in front of the fly. To optogenetically activate or silence 9A neurons, we expressed CsChrimson[74] or GtACR1 (refs. 75,76) in the neurons and used a red laser (638 nm; Laserland) or a green laser (532 nm, CST DPSS laser; Besram Technology) focused on the base of the left front leg while tracking 3D leg-joint kinematics[23,73]. Previous experiments indicate that this optogenetic stimulation affects mostly neurons in the neuromere of the left front leg[73], although we cannot exclude effects on other VNC neurons. The lasers were pulsed at 1,200 Hz with a 60% duty cycle and a resulting power of around 80 mW mm^{-2} at the target. Fly behaviour was recorded in 2-s trials. The laser stimulus began at 0.5 s and lasted 1.0 s.

We used a previously described camera set-up[70] to record the movements of all legs during optogenetic experiments. Six cameras (Basler acA800-510; Basler) equipped with a macro zoom lens (Computar MLM3X-MP; Edmund Optics) were distributed evenly around the fly. We used a previously trained DeepLabCut network[70] to automatically track all leg joints in each camera view. The 2D tracking data from all camera views were combined to reconstruct leg-joint positions and angles in 3D using Anipose[70]. Step cycles were classified automatically on the basis of thresholds on the velocity of the leg tips, as described previously[77]. We focused our analysis on trials in which animals walked forwards (mean forward velocity of at least 5 mm s^{-1} and mean angular velocity of up to 400 deg s^{-1}).

Connectome analyses

Reconstructing FeCO axons and presynaptic neurons. Neurons in the FANC electron-microscopy dataset[78] were previously segmented in an automated manner[7]. To manually correct the automated segmentation of claw and hook axons and their presynaptic neurons, we used Google's collaborative Neuroglancer interface (https://github.com/google/neuroglancer). Presynaptic and postsynaptic neurons that made fewer than three synapses with a neuron of interest were excluded from connectivity analyses. Neuron annotations were managed by the Connectome Annotation Versioning Engine (CAVE) through CAVEclient[79].

Identification of hemilineages and fast-acting neurotransmitters. In *Drosophila*, neurons that share a developmental origin (that is, belong to the same hemilineage) have common anatomical features[29] and release the same fast-acting neurotransmitter[30]. We took advantage of this knowledge to identify the hemilineage, and thus the fast-acting neurotransmitter, of each VNC neuron presynaptic to the claw and hook axons in the FANC connectome. For identification, we used light-smicroscopy images of sparse GAL4 lines[30,64], cell body position along the dorsal–ventral axis and personal communication (from James W. Truman, David Shepherd, Haluk Lacin and Elizabeth Marin). For the descending neurons of interest, we used neurotransmitter predictions[80] of the matched descending neurons in the MANC connectome[81].

Definition of neuron types in FANC. Neurons presynaptic to the 9A neurons in the FANC connectome were identified as sensory neurons, descending neurons or premotor neurons. Sensory neurons had processes entering the VNC from peripheral nerves and no cell body in the VNC. Descending neurons had a process in the neck connective and no cell body in the VNC. Premotor neurons were presynaptic to leg motor neurons in the neuromere of the left front leg. Premotor neurons were previously annotated in ref. 82.

Circuit analysis in MANC. The male adult nerve cord (MANC) connectome[8] and its annotations[9,36] were queried using neuPrint[83]. Neurons that made fewer than five synapses with a neuron of interest were excluded from connectivity analyses.

Circuit analysis in FAFB/FlyWire. The FAFB/FlyWire connectome[38,39] and its annotations[40] were queried using CAVEclient[79] and FAFBseg[38–40]. Neurons that made fewer than five synapses with DNg74 were excluded from connectivity analyses. To analyse the inputs of DNg74 from different brain neuropils, we first calculated the relative number of input synapses of each presynaptic neuron in those neuropils (pooled across hemispheres). The relative synapse counts were then multiplied with the number of synapses between each presynaptic neuron and DNg74. Finally, the weighted synapse counts were summed per neuropil.

Connectome-constrained modelling in MANC. To predict the effects of descending neurons on the activity of chief 9A neurons, we ran a leaky integrate-and-fire model[42] on the MANC connectome[8,9]. Model details are described in ref. 42. In brief, the model uses the entire connectivity of the male VNC and assigns positive or negative weight to each connection, based on the number of synapses between neurons and the predicted neurotransmitter[80] of the presynaptic neuron. We adopted the simulation parameters from ref. 42, including the assumption that acetylcholine has an excitatory effect and that GABA and glutamate have an inhibitory effect. The intrinsic spike rate of the neurons in the model is zero. The descending neurons of interest were stimulated by adding a Poisson spike train of defined frequency. We stimulated the neurons of interest at 50 Hz, 100 Hz or 150 Hz for 1 s per trial. We simulated 30 trials per condition. The resulting spike rate of chief 9A was averaged across the 30 trials per condition.

Reporting summary

Further information on research design is available in the Nature Portfolio Reporting Summary linked to this article.

Data availability

Calcium imaging and behavioural data generated for this study are available from Dryad at https://doi.org/10.5061/dryad.gqnk98t16 (ref. 84). FANC data were analysed from CAVE materialization v.840, timestamp 2024-01-17T08:10:01.179472. MANC data were analysed from v.1.0. FAFB/FlyWire data were analysed from v.783 with synapse predictions from ref. 85.

Code availability

Analyses were done in Matlab 2023a and Python 3.9. Code to recreate the figures is available at GitHub (https://github.com/chrisjdallmann/feco-inhibition). Python code made use of CAVEclient, neuPrint and FAFBseg to interact with the connectomes, NAVis and flybrains to visualize neurons, Brian 2 to simulate neural activity, SciPy for statistics, and Matplotlib, seaborn, NumPy and pandas for general computation and data visualization.

61. Bogovic, J. A. et al. An unbiased template of the *Drosophila* brain and ventral nerve cord. *PLoS ONE* **15**, e0236495 (2020).
62. Schindelin, J. et al. Fiji: an open-source platform for biological-image analysis. *Nat. Methods* **9**, 676–682 (2012).
63. Jenett, A. et al. A GAL4-driver line resource for *Drosophila* neurobiology. *Cell Rep.* **2**, 991–1001 (2012).
64. Meissner, G. W. et al. A searchable image resource of *Drosophila* GAL4 driver expression patterns with single neuron resolution. *eLife* **12**, e80660 (2023).
65. Davie, K. et al. A single-cell transcriptome atlas of the aging *Drosophila* brain. *Cell* **174**, 982–998 (2018).
66. Chen, C.-L. et al. Imaging neural activity in the ventral nerve cord of behaving adult *Drosophila*. *Nat. Commun.* **9**, 4390 (2018).
67. Hermans, L. et al. Microengineered devices enable long-term imaging of the ventral nerve cord in behaving adult *Drosophila*. *Nat. Commun.* **13**, 5006 (2022).
68. Moore, R. J. D. et al. FicTrac: a visual method for tracking spherical motion and generating fictive animal paths. *J. Neurosci. Methods* **225**, 106–119 (2014).
69. Mathis, A. et al. DeepLabCut: markerless pose estimation of user-defined body parts with deep learning. *Nat. Neurosci.* **21**, 1281–1289 (2018).
70. Karashchuk, P. et al. Anipose: a toolkit for robust markerless 3D pose estimation. *Cell Rep.* **36**, 109730 (2021).
71. Guizar-Sicairos, M., Thurman, S. T. & Fienup, J. R. Efficient subpixel image registration algorithms. *Opt. Lett.* **33**, 156–158 (2008).
72. Weir, P. T. & Dickinson, M. H. Functional divisions for visual processing in the central brain of flying *Drosophila*. *Proc. Natl Acad. Sci. USA* **112**, E5523–E5532 (2015).
73. Azevedo, A. W. et al. A size principle for recruitment of *Drosophila* leg motor neurons. *eLife* **9**, e56754 (2020).
74. Klapoetke, N. C. et al. Independent optical excitation of distinct neural populations. *Nat. Methods* **11**, 338–346 (2014).
75. Mohammad, F. et al. Optogenetic inhibition of behavior with anion channelrhodopsins. *Nat. Methods* **14**, 271–274 (2017).
76. Govorunova, E. G., Sineshchekov, O. A., Janz, R., Liu, X. & Spudich, J. L. Natural light-gated anion channels: a family of microbial rhodopsins for advanced optogenetics. *Science* **349**, 647–650 (2015).
77. Pratt, B. G., Lee, S.-Y. J., Chou, G. M. & Tuthill, J. C. Miniature linear and split-belt treadmills reveal mechanisms of adaptive motor control in walking Drosophila. *Curr. Biol.* **34**, 4368–4381 (2024).
78. Phelps, J. S. et al. Reconstruction of motor control circuits in adult *Drosophila* using automated transmission electron microscopy. *Cell* **184**, 759–774 (2021).
79. Dorkenwald, S. et al. CAVE: Connectome Annotation Versioning Engine. *Nat. Methods* **22**, 1112–1120 (2025).
80. Eckstein, N. et al. Neurotransmitter classification from electron microscopy images at synaptic sites in *Drosophila melanogaster*. *Cell* **187**, 2574–2594 (2024).
81. Stürner, T. et al. Comparative connectomics of Drosophila descending and ascending neurons. *Nature* **643**, 158–172 (2025).
82. Lesser, E. et al. Synaptic architecture of leg and wing premotor control networks in *Drosophila*. *Nature* **631**, 369–377 (2024).
83. Plaza, S. M. et al. neuPrint: an open access tool for EM connectomics. *Front. Neuroinform.* **16**, 896292 (2022).
84. Dallmann, C. J. et al. Data from: Selective presynaptic inhibition of leg proprioception in behaving *Drosophila*. *Dryad* https://doi.org/10.5061/dryad.gqnk98t16 (2025).
85. Buhmann, J. et al. Automatic detection of synaptic partners in a whole-brain *Drosophila* electron microscopy data set. *Nat. Methods* **18**, 771–774 (2021).

Acknowledgements We thank members of the Tuthill laboratory for technical assistance and feedback on the manuscript, in particular S.-Y. Lee for help with pilot experiments; K. Eichler and G. Jefferis for help identifying descending neurons; J. M. Ache, O. M. Ahmed, E. Azim, E. M. Chiappe and L. Zhang for feedback on the manuscript; J. S. Phelps, W.-C. A. Lee and the FANC community for contributions to proofreading the FANC connectome; and J. W. Truman and S. S. Bidaye for sharing *Drosophila* stocks. We used stocks obtained from the Bloomington *Drosophila* Stock Center (NIH P40OD018537). This work was supported by a postdoctoral research fellowship from the Deutsche Forschungsgemeinschaft (DFG, German Research Foundation) project 432196121 to C.J.D; NIH grant K99NS117657 to S.A.; and a Searle Scholar Award, a Klingenstein-Simons Fellowship, a Pew Biomedical Scholar Award, a McKnight Scholar Award, a Sloan Research Fellowship, the New York Stem Cell Foundation and NIH grants R01NS102333 and U19NS104655 to J.C.T. J.C.T. is a New York Stem Cell Foundation Robertson Investigator.

Author contributions C.J.D. and J.C.T. conceived the study. C.J.D. developed the set-up and analysis tools for calcium imaging in behaving animals. C.J.D. collected and analysed calcium imaging data for sensory and 9A neurons in behaving animals. Y.L. collected and analysed calcium imaging data for DNg74 neurons. S.A. collected and analysed calcium imaging data for hook neurons during passive leg movements. G.M.C. collected and analysed optogenetic data from flies on the treadmill. A.M. collected and analysed calcium imaging data for hook neurons during optogenetic activation of descending neurons. C.J.D., A.M. and A.S. made

genetic reagents. A.S. acquired confocal images. C.J.D., S.A. and A.C. reconstructed neurons in FANC. C.J.D. and B.W.B. developed computational models. C.J.D. analysed connectome and transcriptome data. C.J.D. visualized the results. C.J.D., S.A. and J.C.T. acquired funding. J.C.T. supervised the project. C.J.D. and J.C.T. wrote the manuscript with input from other authors.

Competing interests The authors declare no competing interests.

Additional information

Supplementary information The online version contains supplementary material available at https://doi.org/10.1038/s41586-025-09554-2.

Correspondence and requests for materials should be addressed to John C. Tuthill.

Peer review information *Nature* thanks the anonymous reviewers for their contribution to the peer review of this work.

Extended Data Fig. 1 | Cell-type specific genetic driver lines. Confocal images showing the expression patterns of the GAL4 and split-GAL4 driver lines used to target FeCO neurons, 9A neurons, and DNg74 neurons. Green, GFP or mVenus; magenta, neuropil stain (nc82). Images of the claw line, the hook flexion line 1, and the DNg74 line are from FlyLight. In the neuromere of each front leg, the claw line targets about 25 axons, each hook line targets about 5 axons, the club line targets about 40 axons, and the 9A line targets about 10 neurons. The DNg74 line targets a single pair of descending neurons. Claw, hook, and club neurons are cholinergic[21]; 9A neurons[30] and DNg74 neurons[80] are GABAergic.

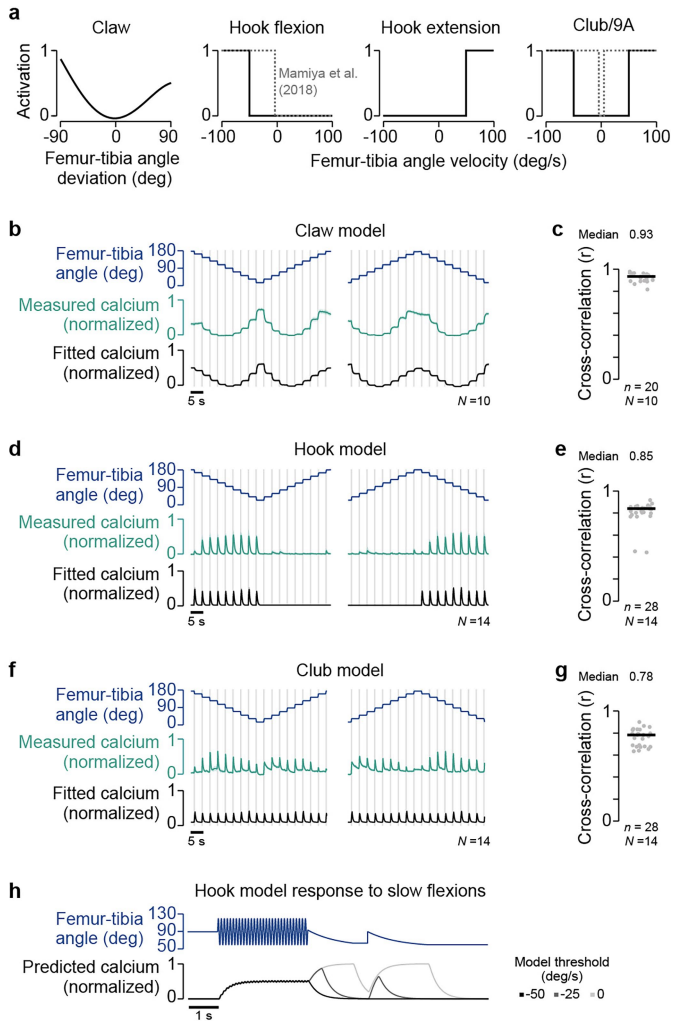

Extended Data Fig. 2 | Computational models for predicting calcium signals in neurons. a, Activation functions for claw, hook flexion, hook extension, and club and 9A neurons. **b**, Measured and fitted calcium signals of claw axons in response to applied ramp-and-hold movements of the femur-tibia joint ($N = 10$ flies per ramp-and-hold stimulus). Lines, mean of animal means; shadings, s.e.m. **c**, Cross-correlation between measured and fitted calcium signals at a time lag of zero ($N = 10$ flies, $n = 20$ trials in total). Black line, median. **d**, Same as **b** but for hook flexion axons ($N = 14$ flies). **e**, Same as **c** but for hook flexion axons ($N = 14$ flies, $n = 28$ trials in total). **f**, Same as **b** but for club axons ($N = 14$ flies). **g**, Same as **c** but for club axons ($N = 14$ flies, $n = 28$ trials in total). **h**, Response of the hook flexion model to an artificial femur-tibia joint angle without tracking noise. When the velocity threshold is larger than −50 deg/s, the model starts to predict strong calcium signals in response to slow flexions, as seen in the measured calcium signals. In **b**–**g**, experimental data are from ref. 21.

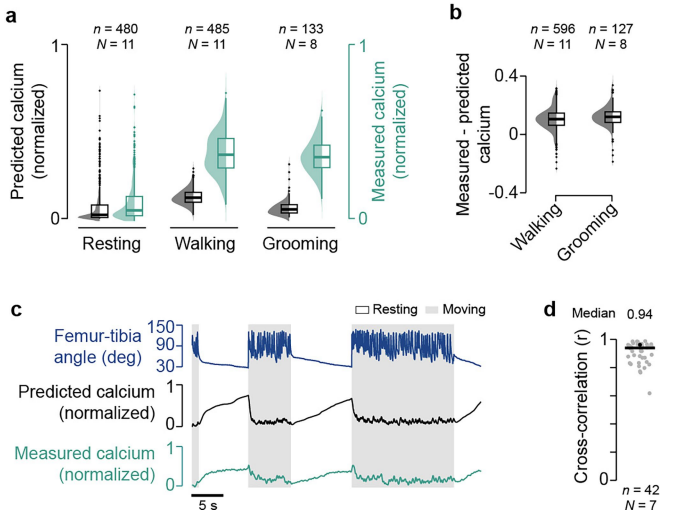

Extended Data Fig. 3 | Calcium signals in claw axons. a, Median predicted and measured calcium signals in claw axons during resting, walking, and grooming on the treadmill (N = 8–11 flies, n = 133–480 bouts in total); bouts are at least 1 s in duration. Note that the calcium signals are smaller than 1 because they are normalized to the largest signal in the dataset, which occurred when the treadmill was removed (data not shown here). **b**, Difference between the absolute mean measured calcium signals and the absolute mean predicted calcium signal in the 0.5 s following transitions into and out of walking or grooming. **c**, Example of calcium imaging of claw axons in the neuromere of the left front leg without the treadmill. **d**, Cross-correlation between predicted and measured calcium signals per trial at a time lag of zero (N = 7 flies, n = 42 trials in total). Black line, median; black dot, trial shown in **c**. In **a** and **b**, distributions show kernel density estimations; boxes show IQR and median, whiskers extend up to 1.5 × IQR.

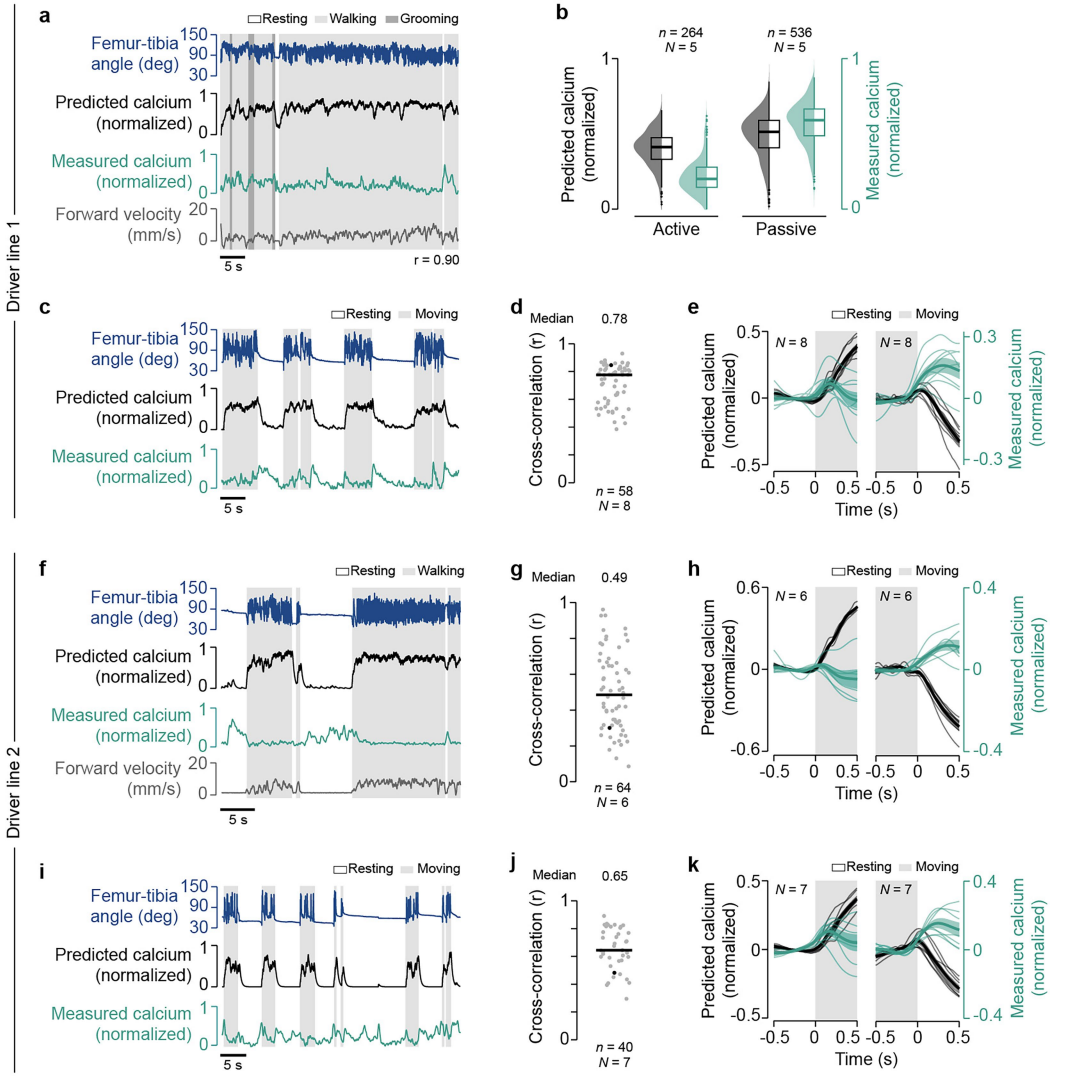

Extended Data Fig. 4 | Calcium signals in hook flexion axons. a, Example trial of calcium imaging of hook flexion axons on the treadmill in which the animal did not transition often between moving and not moving, resulting in a high cross-correlation between predicted and measured calcium signals. **b**, Median predicted and measured calcium signals during active and passive movement bouts on the platform ($N = 5$ flies, $n = 264–536$ bouts in total); bouts are at least 0.5 s in duration. Distributions, kernel density estimations; boxes, IQR and median, whiskers extend up to 1.5 × IQR. **c**, Example of calcium imaging of hook flexion axons without the treadmill. **d**, Cross-correlation between predicted and measured calcium signals per trial at a time lag of zero ($N = 8$ flies, $n = 58$ trials in total). Black line, median; black dot, trial shown in **c**. **e**, Predicted and measured calcium signals aligned to the transitions into and out of movement ($N = 8$ flies). Signals are baseline subtracted (mean from −0.5 to 0 s). Thin lines, animal means; thick lines, mean of means; shadings, s.e.m. **f**, Example calcium imaging of hook flexion axons (second driver line) during behavior on the treadmill. **g**, Same as **d** but for the second hook flexion driver line imaged on the treadmill ($N = 6$ flies, $n = 64$ trials in total). **h**, Same as **e** but for the second hook flexion driver line imaged on the treadmill ($N = 6$ flies). Movement includes walking and grooming. **i**, Example of calcium imaging of hook flexion axons (second driver line) without the treadmill. **j**, Same as **d** but for the second hook flexion driver line imaged without the treadmill ($N = 7$ flies, $n = 40$ trials in total). **k**, Same as **e** but for the second hook flexion driver line imaged without the treadmill ($N = 7$ flies).

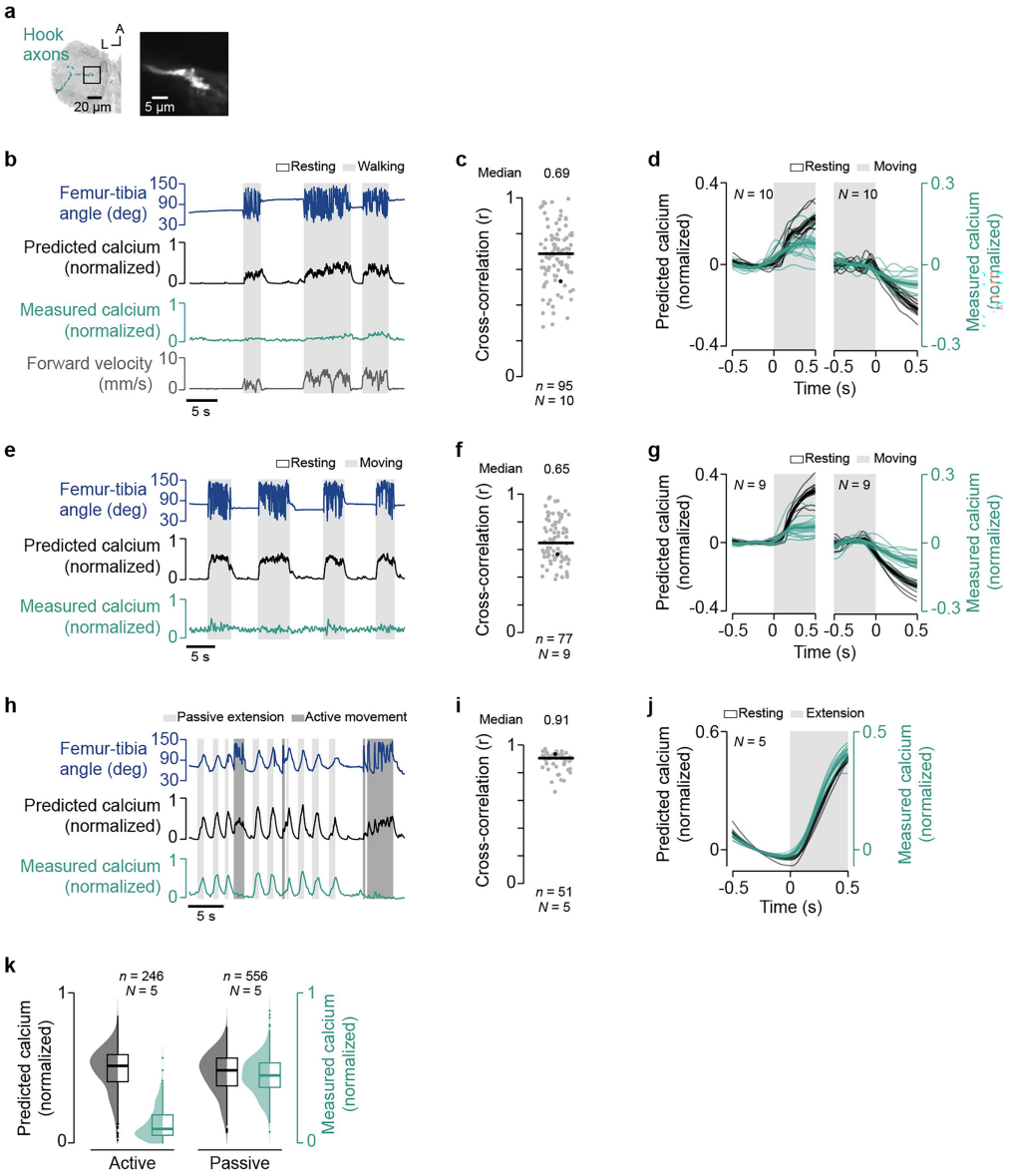

Extended Data Fig. 5 | Calcium signals in hook extension axons. a, Left, confocal image of hook extension axons in the neuromere of the left front leg. Black box, imaging region; green, GFP; gray, neuropil stain (nc82); A, anterior; L, left. Right, mean tdTomato signal of a representative trial. Expression was consistent across animals ($N = 15$). **b**, Example of calcium imaging of hook extension axons during behavior on the treadmill. **c**, Cross-correlation between predicted and measured calcium signals per trial at a time lag of zero ($N = 10$ flies, $n = 95$ trials in total). Black line, median; black dot, trial shown in **b**. **d**, Predicted and measured calcium signals aligned to the transitions into and out of movement ($N = 10$ flies). Movement includes walking and grooming. Signals are baseline subtracted (mean from −0.5 to 0 s). Thin lines, animal means; thick lines, mean of means; shadings, s.e.m. **e**, Example of calcium imaging of hook extension axons without the treadmill. **f**, Same as **c** but for hook extension axons imaged without the treadmill ($N = 9$ flies, $n = 77$ trials in total). **g**, Same as **d** but for hook extension axons imaged without the treadmill ($N = 9$ flies). **h**, Example of calcium imaging of hook extension axons during behavior on the platform. **i**, Same as **c** but for hook extension axons imaged during platform trials ($N = 5$ flies, $n = 51$ trials in total). Active movements were excluded for the cross-correlation. **j**, Same as **d** but for hook extension axons imaged during platform trials ($N = 5$ flies). **k**, Median predicted and measured calcium signals during active and passive movement bouts on the platform ($N = 5$ flies, $n = 246$–556 bouts in total); bouts are at least 0.5 s in duration. Distributions, kernel density estimations; boxes, IQR and median, whiskers extend up to 1.5 × IQR.

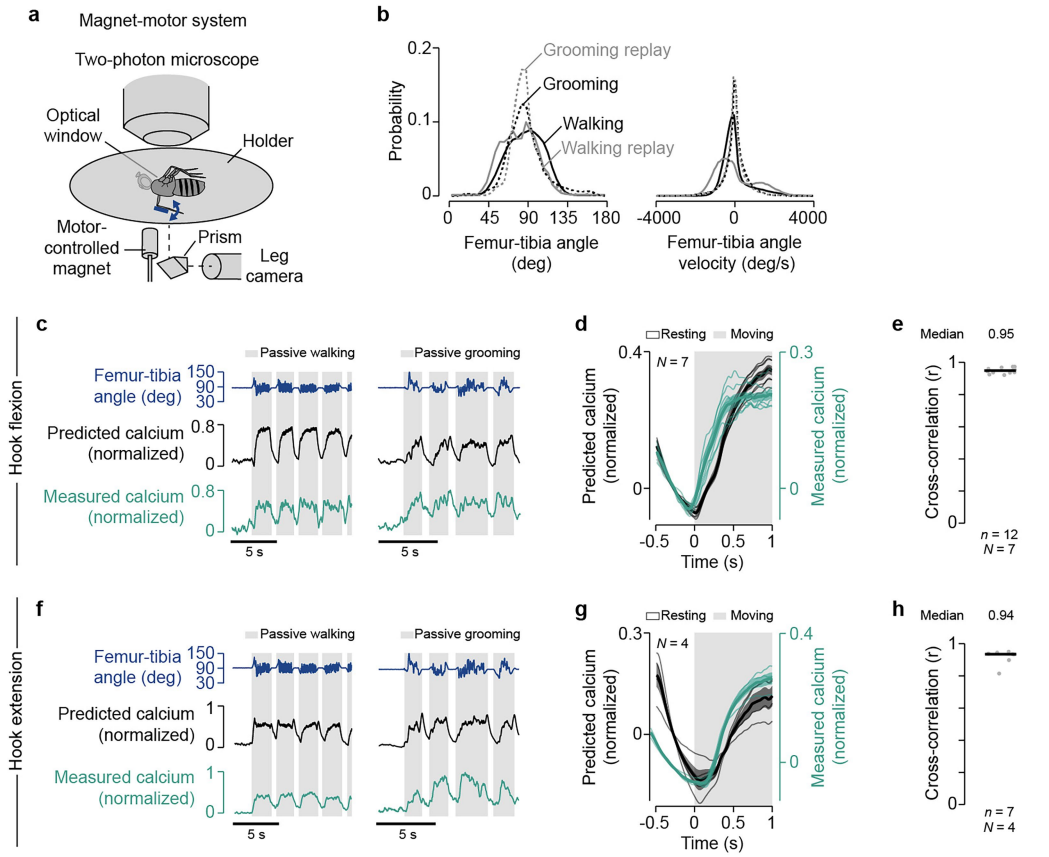

Extended Data Fig. 6 | Calcium signals in hook axons in response to passive leg movements resembling walking and grooming. a, Experimental setup for two-photon calcium imaging from neurons in the neuromere of the left front leg while a front leg tibia is passively moved with a magnet-motor system. **b**, Probability distributions of walking and grooming kinematics recorded in the hook flexion neuron dataset and the walking and grooming kinematics used for passive replay with the setup shown in **a**. **c**, Example of calcium imaging of hook flexion axons during passive tibia movements. **d**, Predicted and measured calcium signals aligned to the transition into passive movement ($N = 7$ flies). Movement includes passive walking and grooming. Signals are baseline subtracted (mean from −0.5 to 0 s). Thin lines, animal means; thick lines, mean of means; shadings, s.e.m. **e**, Cross-correlation between predicted and measured calcium signals per trial at a time lag of zero ($N = 7$ flies, $n = 12$ trials in total). Trials are either walking or grooming replay. Black line, median. **f**, Same as **c** but for hook extension axons. **g**, Same as **d** but for hook extension axons ($N = 4$ flies). **h**, Same as **e** but for hook extension axons ($N = 4$ flies, $n = 7$ trials in total).

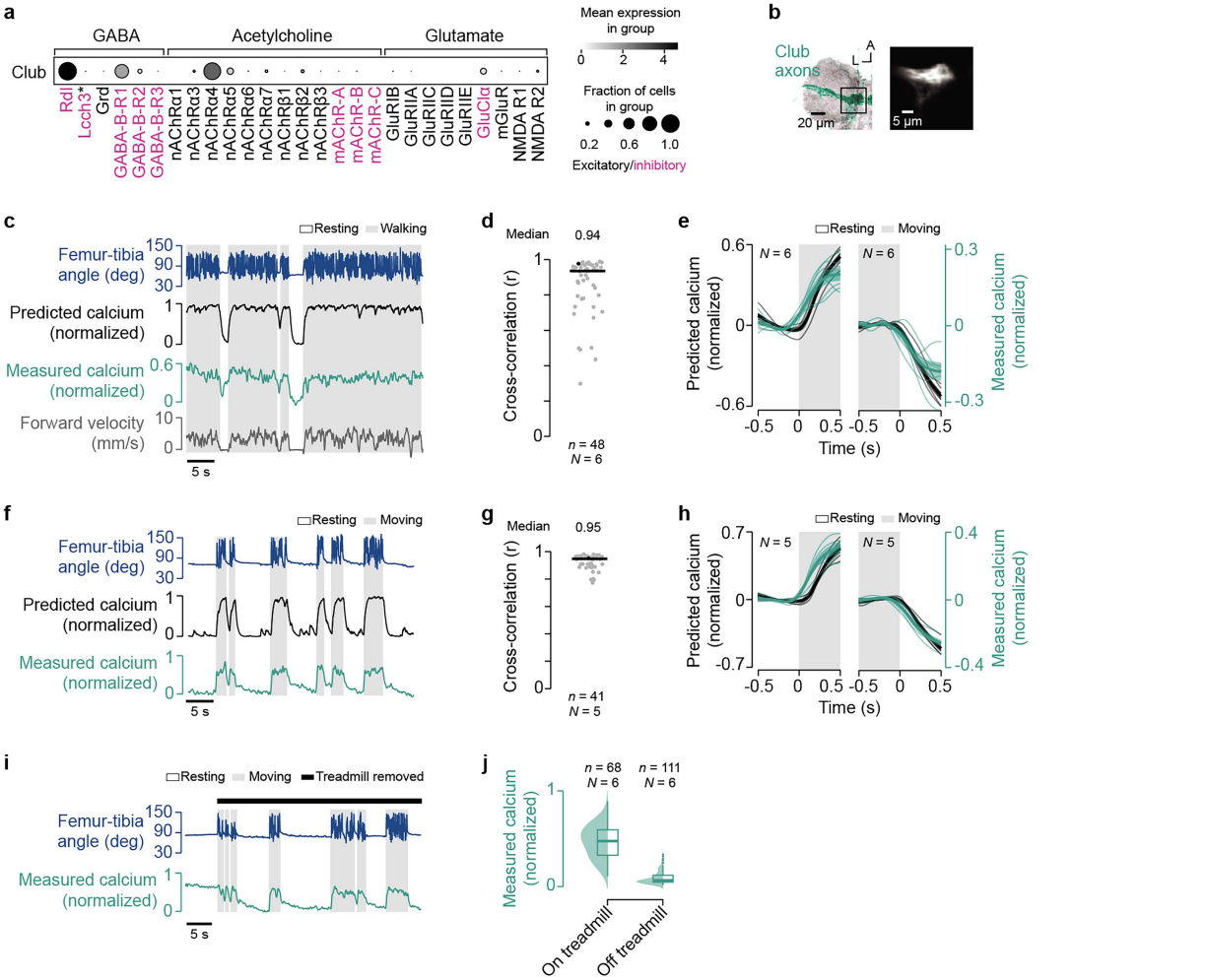

Extended Data Fig. 7 | RNA-seq data for club neurons and calcium signals in club axons. a, Expression levels of receptor genes in club neurons. **b**, Left, confocal image of club axons in the neuromere of the left front leg. Black box, imaging region; green, GFP; gray, neuropil stain (nc82); A, anterior; L, left. Right, mean tdTomato signal of a representative trial. Expression was consistent across animals ($N = 6$). **c**, Example of calcium imaging of club axons during behavior on the treadmill. **d**, Cross-correlation between predicted and measured calcium signals per trial at a time lag of zero ($N = 6$ flies, $n = 48$ trials in total). Black line, median; black dot, trial shown in **c**. **e**, Predicted and measured calcium signals aligned to the transitions into and out of movement ($N = 6$ flies). Movement includes walking and grooming. Signals are baseline subtracted (mean from −0.5 to 0 s). Thin lines, animal means; thick lines, mean of means; shadings, s.e.m. **f**, Example of calcium imaging of club axons without the treadmill. **g**, Same as **d** but for club axons imaged without the treadmill ($N = 5$ flies, $n = 41$ trials in total). **h**, Same as **e** but for club axons imaged without the treadmill ($N = 5$ flies). **i**, Example of calcium imaging of club axons in which the treadmill was lowered out of reach for the fly after 5 s. **j**, Median calcium signals during resting bouts on and off the treadmill ($N = 6$ flies, $n = 68$–111 bouts in total); bouts are at least 1 s in duration. Distributions, kernel density estimations; boxes, IQR and median, whiskers extend up to 1.5 × IQR.

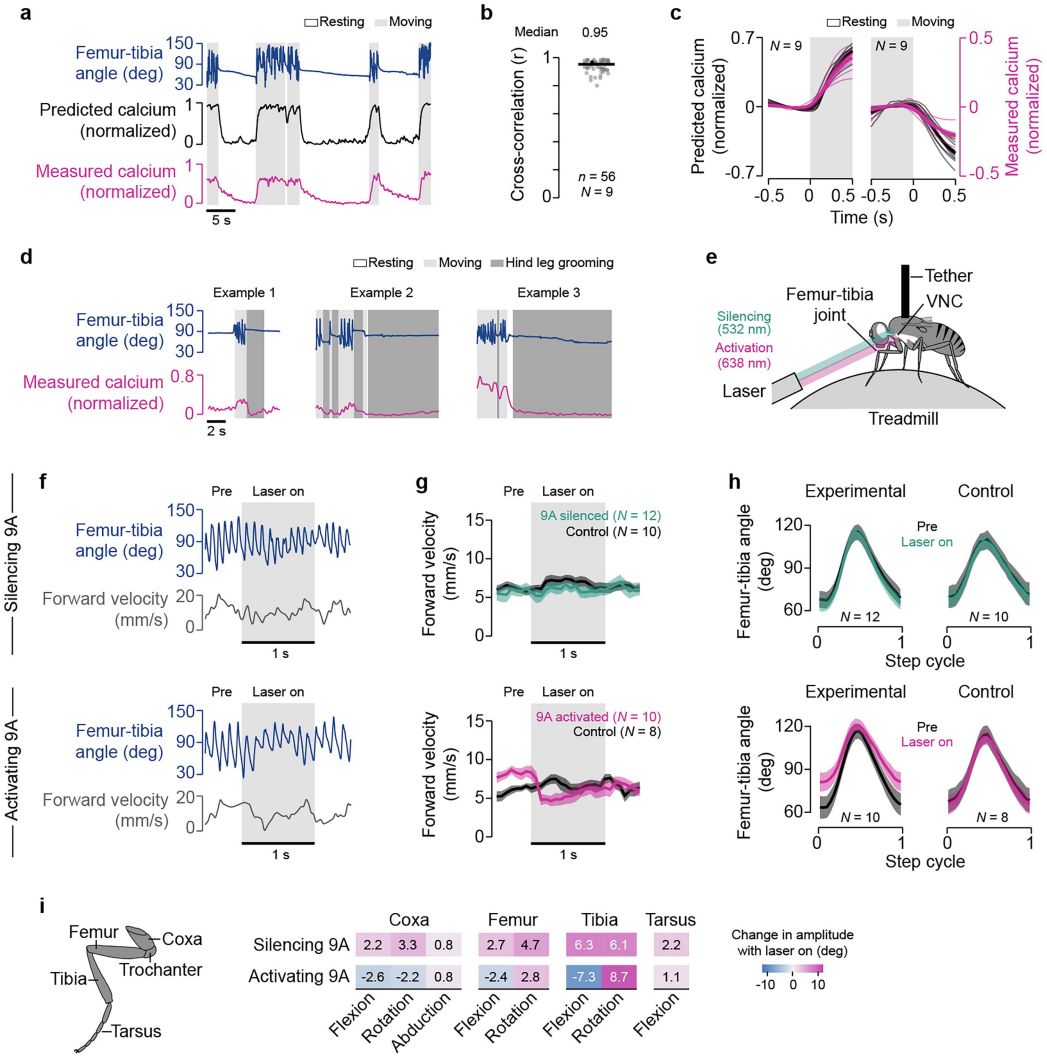

Extended Data Fig. 8 | Calcium imaging and optogenetic manipulation of 9A neurons. a, Example of calcium imaging of 9A neurons in the neuromere of the left front leg without the treadmill. **b**, Cross-correlation between predicted and measured calcium signals per trial at a time lag of zero ($N = 9$ flies, $n = 56$ trials in total). Black line, median; black dot, trial shown in **a**. **c**, Predicted and measured calcium signals aligned to the transitions into and out of movement ($N = 9$ flies). Signals are baseline subtracted (mean from −0.5 to 0 s). Thin lines, animal means; thick lines, mean of means; shadings, s.e.m. **d**, Examples of calcium imaging of 9A neurons during hind leg grooming. **e**, Experimental setup for optogenetic activation or silencing of neurons in the neuromere of the left front leg. **f**, Examples of 9A silencing (top) and activation (bottom) in experimental flies walking on the treadmill. **g**, Mean forward velocity of experimental and control flies during the 2 s trials (66.6 ms bins; $N = 10$–12 flies). Thick lines, means of animal means; shadings, s.e.m. **h**, Femur-tibia angle of the left front leg of experimental and control flies normalized in time to the step cycle (0.04 bins; $N = 8$–12 flies). Thick lines, mean of animal means; shadings, s.e.m. **i**, Mean differences in joint angle amplitudes between steps during (laser on) and before (pre) the optogenetic manipulation.

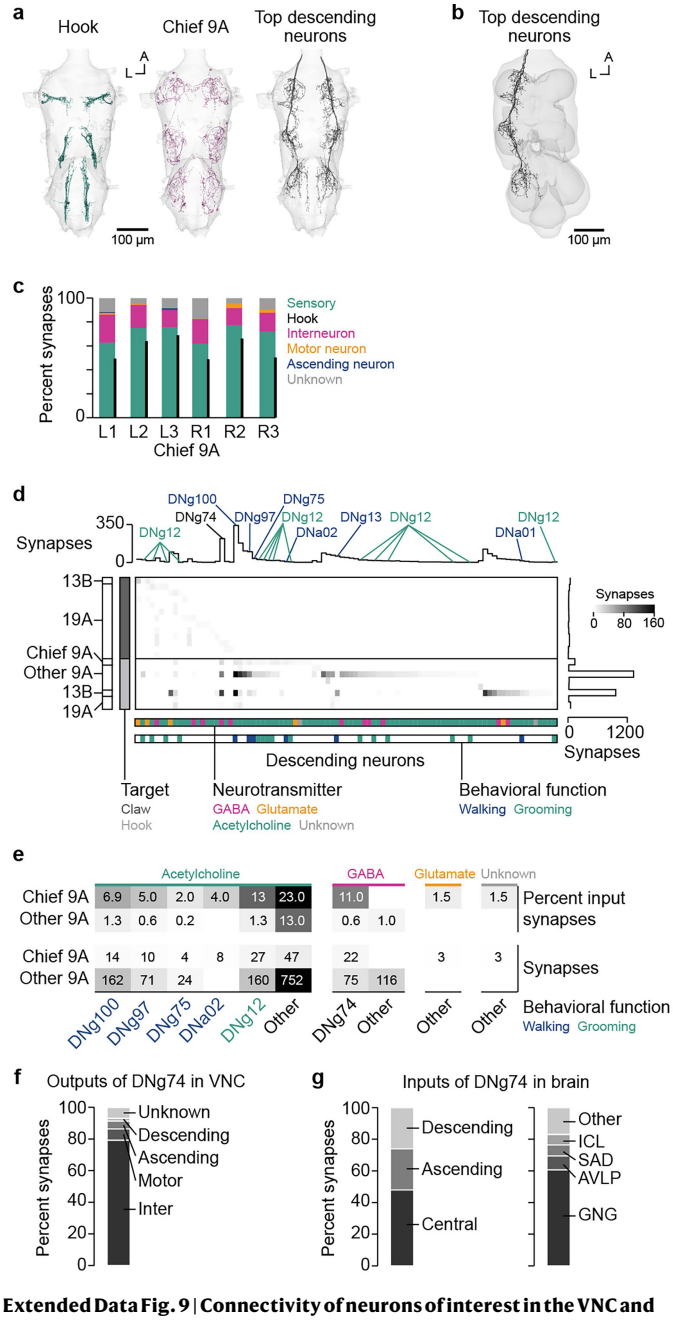

Extended Data Fig. 9 | Connectivity of neurons of interest in the VNC and the brain. a, Hook axons, chief 9A neurons presynaptic to hook axons, and the top two descending neurons presynaptic to the chief 9A neurons in the male VNC connectome (MANC). A, anterior; L, left. **b**, Top two descending neurons presynaptic to the chief 9A neuron in the female VNC connectome (FANC). **c**, Outputs of chief 9A neurons onto different neuron types (MANC connectome). Black bars, output onto hook axons; L, left side of VNC; R, right side of VNC; 1, front leg neuromere; 2, middle leg neuromere; 3, hind leg neuromere. **d**, Connectivity of descending neurons with GABAergic neurons presynaptic to claw and hook axons. Descending neurons known to drive walking and grooming are indicated. Neurotransmitter predictions are from matched descending neurons in MANC[81]. **e**, Connectivity between descending neurons and 9A neurons. Numbers indicate connection strength to 9A as percent input synapses (top two rows) or absolute synapses (bottom two rows). Synapses from all DNg12 were summed. For "Other 9A" neurons, percent input synapses were averaged and absolute synapses were summed. **f**, Outputs of DNg74 in the VNC (MANC connectome). **g**, Inputs of DNg74 in the brain (FlyWire connectome). GNG, gnathal ganglia; AVLP, anterior ventrolateral protocerebrum; SAD, saddle; ICL, inferior clamp.

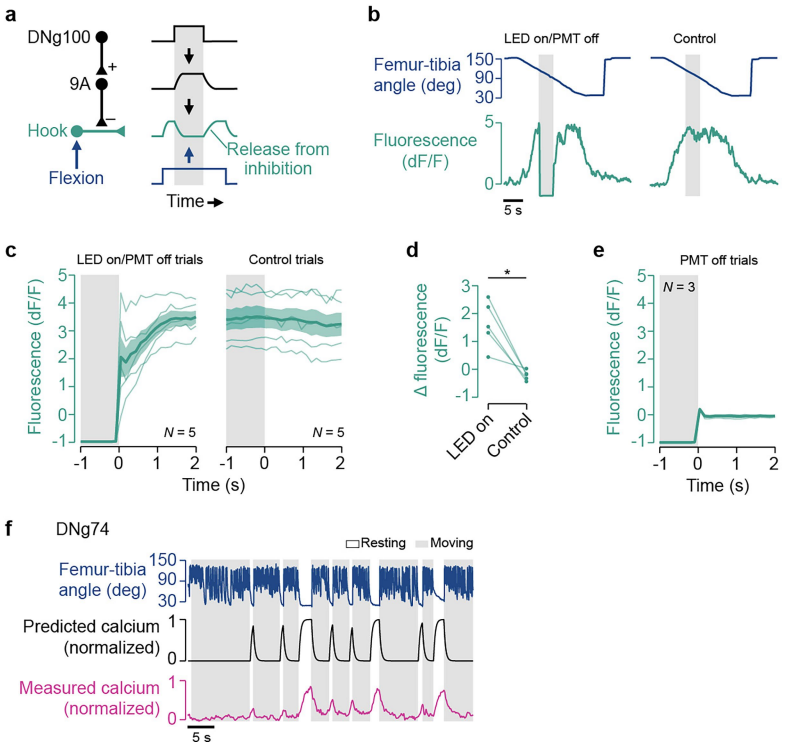

Extended Data Fig. 10 | Calcium signals in hook axons in response to DNg100 activation and calcium signals in DNg74. a, Expected indirect inhibitory effect of DNg100 activation onto hook axons. **b**, Examples showing hook flexion responses with and without optogenetic activation of DNg100. During the activation (gray, left), the PMT of the microscope was switched off, as indicated by a sudden drop in fluorescence. **c**, Calcium signals from hook flexion axons aligned to the offset of the LED and the equivalent time point in control trials ($N = 5$ flies, $n = 5$ transitions per fly). Thin lines, animal means; thick lines, mean of means; shadings, s.e.m. Note that the "spike" seen in some calcium signals directly after the offset is an artifact. **d**, Mean change in calcium signals per animal within 2 s after the offset of the LED or the equivalent time point in control trials (two-sided paired t-test, $t(4) = 4.54$, $p = 0.01$). Positive values indicate that calcium signals increased after the offset of the LED. **e**, GFP signals from FeCO axons aligned to switching on the PMT ($N = 3$ flies, $n = 12$ transitions per fly). **f**, Example of calcium imaging of DNg74 in the neuromere of the left front leg without the treadmill.

nature portfolio

Corresponding author(s): John Tuthill

Last updated by author(s): Aug 7, 2025

Reporting Summary

Nature Portfolio wishes to improve the reproducibility of the work that we publish. This form provides structure for consistency and transparency in reporting. For further information on Nature Portfolio policies, see our Editorial Policies and the Editorial Policy Checklist.

Statistics

For all statistical analyses, confirm that the following items are present in the figure legend, table legend, main text, or Methods section.

n/a	Confirmed
☐	☒ The exact sample size (*n*) for each experimental group/condition, given as a discrete number and unit of measurement
☐	☒ A statement on whether measurements were taken from distinct samples or whether the same sample was measured repeatedly
☐	☒ The statistical test(s) used AND whether they are one- or two-sided *Only common tests should be described solely by name; describe more complex techniques in the Methods section.*
☒	☐ A description of all covariates tested
☒	☐ A description of any assumptions or corrections, such as tests of normality and adjustment for multiple comparisons
☐	☒ A full description of the statistical parameters including central tendency (e.g. means) or other basic estimates (e.g. regression coefficient) AND variation (e.g. standard deviation) or associated estimates of uncertainty (e.g. confidence intervals)
☐	☒ For null hypothesis testing, the test statistic (e.g. *F*, *t*, *r*) with confidence intervals, effect sizes, degrees of freedom and *P* value noted *Give P values as exact values whenever suitable.*
☒	☐ For Bayesian analysis, information on the choice of priors and Markov chain Monte Carlo settings
☒	☐ For hierarchical and complex designs, identification of the appropriate level for tests and full reporting of outcomes
☒	☐ Estimates of effect sizes (e.g. Cohen's *d*, Pearson's *r*), indicating how they were calculated

Our web collection on statistics for biologists contains articles on many of the points above.

Software and code

Policy information about availability of computer code

Data collection	Matlab (2023a, RRID:SCR_001622), ScanImage (5.2, RRID:SCR_014307), FicTrac (https://github.com/rjdmoore/fictrac)
Data analysis	Matlab (2023a, RRID:SCR_001622), Python (3.9, RRID:SCR_008394), Anipose (1.0.1, RRID:SCR_023041), DeepLabCut (2.3.5, RRID:SCR_021391), CAVEclient (7.6.0, https://github.com/CAVEconnectome/CAVEclient/), neuPrint (0.5.1, https://connectome-neuprint.github.io/neuprint-python/), FAFBseg (3.1.0, https://fafbseg-py.readthedocs.io/), NAVis (1.10.0, https://navis-org.github.io/navis/), flybrains (0.3.0, https://github.com/navis-org/navis-flybrains/), Brian 2 (2.9.0, https://brian2.readthedocs.io/), SciPy (1.15.2, https://scipy.org/), Matplotlib (3.10.1, https://matplotlib.org/), seaborn (0.13.2, https://seaborn.pydata.org/), NumPy (2.2.3, https://numpy.org/), pandas (2.2.3, https://pandas.pydata.org/), Neuroglancer (RRID:SCR_015631), SCope (1.8.2, https://scope.aertslab.org/), FIJI (1.54, RRID:SCR_002285), Computational Morphometry Toolkit (3.4.0, RRID:SCR_002234), custom code (https://github.com/chrisjdallmann/feco-inhibition)

For manuscripts utilizing custom algorithms or software that are central to the research but not yet described in published literature, software must be made available to editors and reviewers. We strongly encourage code deposition in a community repository (e.g. GitHub). See the Nature Portfolio guidelines for submitting code & software for further information.

Data

Policy information about availability of data

All manuscripts must include a data availability statement. This statement should provide the following information, where applicable:

- Accession codes, unique identifiers, or web links for publicly available datasets
- A description of any restrictions on data availability
- For clinical datasets or third party data, please ensure that the statement adheres to our policy

Calcium imaging and behavioral data generated for this study is available for download from Dryad (https://doi.org/10.5061/dryad.gqnk98t16). FANC data were analyzed from CAVE materialization version 840, timestamp 2024-01-17T08:10:01.179472. MANC data were analyzed from version 1.0. FAFB/FlyWire data were analyzed from version 783.

Research involving human participants, their data, or biological material

Policy information about studies with human participants or human data. See also policy information about sex, gender (identity/presentation), and sexual orientation and race, ethnicity and racism.

Reporting on sex and gender	N/A
Reporting on race, ethnicity, or other socially relevant groupings	N/A
Population characteristics	N/A
Recruitment	N/A
Ethics oversight	N/A

Note that full information on the approval of the study protocol must also be provided in the manuscript.

Field-specific reporting

Please select the one below that is the best fit for your research. If you are not sure, read the appropriate sections before making your selection.

☒ Life sciences ☐ Behavioural & social sciences ☐ Ecological, evolutionary & environmental sciences

For a reference copy of the document with all sections, see nature.com/documents/nr-reporting-summary-flat.pdf

Life sciences study design

All studies must disclose on these points even when the disclosure is negative.

Sample size	No sample size calculation was performed. Sample sizes were chosed based on standards in the field (e.g., https://doi.org/10.1038/s41586-024-07854-7, https://www.nature.com/articles/s41586-023-06632-1, https://www.nature.com/articles/s41586-024-07039-2, https://doi.org/10.1038/s41467-022-32571-y).
Data exclusions	Calcium imaging frames were excluded from the analysis if the front leg was involved in movements other than walking or grooming on the treadmill (e.g., pushing), the femur-tibia joint of the front leg was not tracked correctly, or the two-photon image registration failed (e.g., the region of interest moved out of the imaging volume).
Replication	Calcium imaging experiments were performed in 5-11 animals per genotype. Optogenetic experiments were performed in 8-12 animals per genotype. Confocal images were taken from 6-13 animals per genotype. All attempts at replication were successful. The VNC connectome analysis was performed in 2 connectomes. The brain connectome analysis was performed in 1 connectome.
Randomization	Not relevant to our study because we did not have different treatment allocations.
Blinding	Not relevant to our study because we did not have different treatment allocations.

Reporting for specific materials, systems and methods

We require information from authors about some types of materials, experimental systems and methods used in many studies. Here, indicate whether each material, system or method listed is relevant to your study. If you are not sure if a list item applies to your research, read the appropriate section before selecting a response.

Materials & experimental systems

n/a	Involved in the study
☐	☒ Antibodies
☒	☐ Eukaryotic cell lines
☒	☐ Palaeontology and archaeology
☐	☒ Animals and other organisms
☒	☐ Clinical data
☒	☐ Dual use research of concern
☒	☐ Plants

Methods

n/a	Involved in the study
☒	☐ ChIP-seq
☒	☐ Flow cytometry
☒	☐ MRI-based neuroimaging

Antibodies

Antibodies used

Rat anti-CD8 monoclonal antibody (Thermo Fisher Scientific Cat# MCD0800, RRID:AB_10392843, Clone ID 5H10), mouse anti-Bruchpilot monoclonal antibody (DSHB Cat# nc82, RRID:AB_2314866, Clone ID N/A), goat anti-rat secondary antibody Alexa Fluor 488 conjugate (Thermo Fisher Scientific Cat# A-11006, RRID:AB_2534074), goat anti-mouse secondary antibody Alexa Fluor 633 conjugate (Thermo Fisher Scientific Cat# A-21050, RRID:AB_141431).

Validation

All antibodies used in this study are commercially available and have been applied to the Drosophila nervous system in previous studies. Validation information can be found at the manufacturer's website:
Rat anti-CD8 monoclonal antibody: https://www.thermofisher.com/antibody/product/CD8-alpha-Antibody-clone-5H10-Monoclonal/MCD0800.
Mouse anti-Bruchpilot monoclonal antibody: https://dshb.biology.uiowa.edu/nc82.
Goat anti-rat secondary antibody: https://www.thermofisher.com/antibody/product/Goat-anti-Rat-IgG-H-L-Cross-Adsorbed-Secondary-Antibody-Polyclonal/A-11006.
Goat anti-mouse secondary antibody: https://www.thermofisher.com/antibody/product/Goat-anti-Mouse-IgG-H-L-Cross-Adsorbed-Secondary-Antibody-Polyclonal/A-21050.

Animals and other research organisms

Policy information about studies involving animals; ARRIVE guidelines recommended for reporting animal research, and Sex and Gender in Research

Laboratory animals	This study used genetically modified adult female and male Drosophila melanogaster, 1-14 days post-eclosion.
Wild animals	The study did not involve wild animals.
Reporting on sex	The study includes data from male and female Drosophila melanogaster.
Field-collected samples	The study did not involve samples collected from the field.
Ethics oversight	Studies involving Drosophila melanogaster are exempt from ethical approval.

Note that full information on the approval of the study protocol must also be provided in the manuscript.

Plants

Seed stocks	*Report on the source of all seed stocks or other plant material used. If applicable, state the seed stock centre and catalogue number. If plant specimens were collected from the field, describe the collection location, date and sampling procedures.*
Novel plant genotypes	*Describe the methods by which all novel plant genotypes were produced. This includes those generated by transgenic approaches, gene editing, chemical/radiation-based mutagenesis and hybridization. For transgenic lines, describe the transformation method, the number of independent lines analyzed and the generation upon which experiments were performed. For gene-edited lines, describe the editor used, the endogenous sequence targeted for editing, the targeting guide RNA sequence (if applicable) and how the editor was applied.*
Authentication	*Describe any authentication procedures for each seed stock used or novel genotype generated. Describe any experiments used to assess the effect of a mutation and, where applicable, how potential secondary effects (e.g. second site T-DNA insertions, mosiacism, off-target gene editing) were examined.*